P-08-44

Oskarshamn site investigation

Detecting the near surface redox front in crystalline rock

Results from drill cores KLX09B-G and KLX11B-F

Henrik Drake, Department of Geology, Earth Sciences Centre University of Gothenburg

Eva-Lena Tullborg, Terralogica AB

December 2008

Svensk Kärnbränslehantering AB
Swedish Nuclear Fuel
and Waste Management Co

Box 250, SE-101 24 Stockholm
Phone +46 8 459 84 00

SKB

ISSN 1651-4416
SKB P-08-44

Oskarshamn site investigation

Detecting the near surface redox front in crystalline rock

Results from drill cores KLX09B-G and KLX11B-F

Henrik Drake, Department of Geology, Earth Sciences
Centre University of Gothenburg

Eva-Lena Tullborg, Terralogica AB

December 2008

Keywords: Redox, Fracture minerals, Pyrite, Goethite, Chemistry, U-series disequilibrium, SEM-EDS, Stable isotopes, Laxemar.

This report concerns a study which was conducted for SKB. The conclusions and viewpoints presented in the report are those of the authors and do not necessarily coincide with those of the client.

Data in SKB's database can be changed for different reasons. Minor changes in SKB's database will not necessarily result in a revised report. Data revisions may also be presented as supplements, available at www.skb.se.

A pdf version of this document can be downloaded from www.skb.se

Abstract

Oxidising conditions in surface- and near-surface groundwaters normally change to reducing conditions encountered in groundwaters at larger depth. Oxygen originally present is consumed through biogenic and inorganic reactions along the flow paths. Also fracture minerals take part in these reactions and the fracture mineralogy/geochemistry can be used to trace the redox transition zone. To demonstrate that reducing conditions can be maintained for a long period of time is an important task for the safety assessment in the planning of a radioactive waste disposal in crystalline rock. This is because oxygen may cause harm to the copper canisters hosting the waste and oxidising conditions may increase the mobility of some radionuclides in case of leakage of the canister. The present study of the near-surface redox front is carried out using mineralogy (redox sensitive minerals), chemistry (redox sensitive elements) and U-series isotopes. The distribution of the redox sensitive minerals pyrite and goethite in open fractures (sampled from closely spaced, ~100 m deep boreholes) shows that the redox front (switch from mainly goethite to mainly pyrite in the fractures) generally occurs at about 15–20 m depth. Calcite distribution shows leaching of calcite in the upper 20–30 m and positive Ce-anomalies suggest oxidation of Ce down to 20 m depth. The U-series isotopes show disequilibrium in most of the samples indicating mobility of U during the last 1 Ma. In the upper 20 m, U is mainly removed (due to oxidation) or has experienced complex removal and/or deposition. At depths of 35–55 m both deposition and removal of U (occasionally complex) is indicated. Below 55 m, recent deposition of U is generally indicated which suggests removal of U near surface (oxidation) and deposition of U below the redox front (reduction). Scattered goethite occurrences below the redox front (down to 90 m) and signs of U removal at 35–55 m generally correlate with sections of high transmissivity (and/or high fracture frequencies). This shows that highly transmissive fractures are generally required to allow oxygenised groundwaters below the redox transition zone and that recent (< 300 ka) removal of U (oxidation) below 55 m is not detected in the analysed samples. Although penetration of glacial waters to great depths has been confirmed in the study area, these waters have been reduced near the surface.

Sammanfattning

Oxiderande förhållanden i ytvatten och ytliga grundvatten övergår till reducerande förhållanden i grundvattnen på större djup (oftast under 50 till 100 m). Det lösta syret i de ytliga vattnen konsumeras genom olika redox reaktioner längs flödesvägen. Dessa reaktioner kan vara både oorganiska, t.ex. oxidering av sulfider och Fe2+ som finns i olika sprickmineral, eller organiska, t.ex. konsumtion av syre i samband med nedbrytning av organiskt material. Exakt var övergången mellan oxiderande och reducerande förhållanden sker och hur bred denna övergångszon är beror på många olika faktorer såsom; jordlagrens tjocklek och sammansättning, de hydrogeologiska förhållanden, bergart samt sprickornas orientering och beskaffenhet. Att kunna visa på att dessa processer på ett tillfredställande sätt kan ta hand om det lösta syret som kommer in i berget, både nu och i framtiden, är av stor betydelse för säkerhets-bedömningarna i samband med lokaliseringen av ett förvar för använt kärnbränsle. Denna rapport visar hur övergången från oxiderande till reducerande förhållanden i berget kan beläggas med hjälp av olika mineralogiska och geokemiska metoder. Studien har utförts på borrkärnar från två olika borrplatser (KLX09 och KLX11) i delområde Laxemar (Oskarshamns platsundersökningsområde). På dessa platser har 5 respektive 6 stycken ca 100–150 m långa kärnborrhål borrats från ytan i olika riktningar i syfte att få en bra representation av de olika sprickriktningarna. Studien är baserad på mineralogi (frekvens och utbredning av redoxkänsliga mineral som götit, pyrit och kalcit), geokemi (redoxkänsliga element som Ce och U), samt U seriens isotoper).

Contents

1 Introduction

It is important to demonstrate that reducing conditions can be maintained for a long period of time at the depths (~500 m) of a high-level radioactive waste repository /e.g. Gascoyne 1999, Guimerà et al. 1999, Puigdomenech et al. 2001/. This is because oxygen may harm the copper canisters in which the used fuel is contained. Furthermore, in case of canister leakage, oxidising conditions may increase the mobility of some radionuclides, especially U-oxide. Oxidising conditions in surface- and near-surface groundwaters generally change to reducing conditions in deeper groundwaters, by reduction of the oxygen through biogenic and inorganic reactions along the flow paths. These reactions involve fracture minerals, and the fracture filling mineralogy and geochemistry can be used to trace the redox transition zone (front) /Landström et al. 2001 Tullborg et al. 2008/, i.e. the change from oxidising to reducing conditions at depth. The exact position of this front is best exemplified in sedimentary rocks, (e.g. sandstones) which often show distinct colour differences and has only been described from granitic rocks in rare cases /e.g. Akagawa et al. 2006, Yoshida et al. 2006/. Such oxidation-related colour differences are not common in the crystalline basement of Sweden and potential oxidation effects are commonly limited to water-conducting fractures (or fracture zones). In these cases, the only way to recognise a redox front is by using microscopy to evaluate mineralogical effects due to oxidation, and to examine the behaviour of redox sensitive elements.

Information about the recent redox front position in the shallow bedrock and its stability over time is important for the understanding of at what depth recently descending oxygenated waters were reduced. A scenario which may introduce oxygenated water into the bedrock is glacial melt-water which may contain more dissolved oxygen than the present recharge water. Also the organic buffer may be severely reduced below the ice /Puigdomenech et al. 2001/. High hydraulic heads beneath a continental ice sheet may force this oxygen-rich water to great depths in the bedrock. The extent and potential for dissolved oxygen to migrate to great depth in such a glacial scenario is debateable. It is argued that glacial melt-water will not reach the planned depth of the repository in Sweden during its life-time /Gascoyne 1999, Guimerà et al. 1999/.

The present study of the redox front location is carried out in the Laxemar area on the east coast of Sweden (Figure 1-1), an area currently investigated as a potential site for a deep repository for spent nuclear fuel by the Swedish Nuclear Fuel and Waste Management Co. (SKB). The site investigations have resulted in detailed information about the present hydrogeology and hydrochemistry /e.g. SKB 2006/ as well as about the evolution of the bedrock geology /e.g. Wahlgren et al. 2006/, Quaternary deposits /e.g. Rudmark et al. 2005/ and paleohydrogeology (fracture fillings/coatings and wall rock alteration) /e.g. Drake and Tullborg 2007/. The present study is carried out on drill core samples from closely spaced, ~100 m deep boreholes from two different drill sites (at about 20–27 m.a.s.l.). It is mainly focused on detection of the redox front with use of mineralogy (distribution of redox sensitive minerals), chemistry (redox sensitive elements, e.g. Ce, Mn and Fe) and U-series isotopes in fracture coatings (and to a lesser degree the migration of the redox front into the wall rock adjacent to near surface fractures). Since analyses of Fe^{III}/Fe^{II} and Fe isotopes also may give information of the redox front position, as shown at nearby Äspö and Oskarshamn /Dideriksen et al. 2007/ material from the boreholes in the present study are currently being analysed for Fe^{III}/Fe^{II} and Fe isotopes.

Redox sensitive Fe-minerals such as pyrite, Fe-oxides and Fe-oxyhydroxides (FeOOH, e.g. goethite) can be used for detection of the redox front /cf. Landström et al. 1989, Landström et al. 2001/ as shown by detailed mapping of the distribution of these minerals in redox front studies at Äspö close to the Laxemar subarea and at other sites in southern Sweden /Eliasson et al. 1989, Tullborg 1997/. In these studies the redox front position was recognised at various depths (down to 100 m) depending on local topography (affecting recharge/discharge), fracture frequencies and orientations. Oxidation of pyrite, precipitation of goethite, and associated dissolution of calcite were observed near surface. In areas with a thick soil cover, oxidative alteration may not be seen in the bedrock because the groundwater may be reduced by the time it enters the bedrock.

Redox measurements in the groundwater is usually not reliable in the near surface region e.g. due to mixing of waters /Tullborg et al. 2008/. However, redox conditions can be evaluated by examining redox sensitive elements like Ce and U in minerals deposited along the fracture flow paths. Since, oxidised Ce (Ce^{IV}) is less mobile than Ce^{III}, lake and stream waters usually show negative Ce-anomalies /cf. Dia et al. 2000, Rönnback et al. 2008/. Both positive and negative Ce-anomalies can be found in minerals close to the surface, e.g. due to in situ oxidation of Ce on mineral surfaces /Landström and Tullborg 1995, Bau 1999, Takahashi et al. 2000/ and due to precipitation from water with negative Ce-anomalies /Landström and Tullborg 1989, Vaniman and Chipera 1996, Milodowski et al. 2005/, respectively.

Although the position of the redox front can be detected by distribution of redox sensitive minerals and elements, this information provides no time constraints. Thus it is a question whether the redox front corresponds to the present conditions. However, time constraints of oxidising and reducing conditions in the bedrock fractures can be achieved by measurements of isotopes in the U-series decay chain (^{238}U-^{234}U-^{230}Th, /e.g. MacKenzie et al. 1992, Suksi and Rasilainen 2002, Tullborg et al. 2003, Min et al. 2005/. This method is able to trace deposition or removal of U within the last ~300 ka (^{234}U-^{230}Th) or 1 Ma (^{238}U-^{234}U), after which the nuclides in the decay chain approach secular equilibrium, i.e. their activity ratios (AR) equal 1±0.1 /Osmond and Ivanovich 1992, Gascoyne et al. 2002/. Oxidation of U^{IV} to the more mobile U^{VI} commonly generates leaching of U at shallow depths /e.g. Landström et al. 2001/ and a higher U content in surface water than in deeper groundwater /e.g. SKB 2004/. Since both ^{238}U and ^{234}U are leached by oxidative fluids and Th is much less mobile than U, recent removal of U (oxidising conditions) results in $^{234}U/^{238}U$ AR ~1 and $^{230}Th/^{234}U$ AR <1 in the groundwater and $^{230}Th/^{234}U$ AR > 1 in the solid phase. At reducing conditions (greater depths) ^{234}U is leached more easily than ^{238}U because ^{234}U is usually in the state of U^{VI} due to recoil effects while ^{238}U is usually reduced to U^{IV} and less mobile /e.g. Suksi and Rasilainen 2002/. Groundwater in the bedrock usually has $^{234}U/^{238}U$ AR > 1 /e.g. Tullborg et al. 2003/ and the AR is inherited by U deposited in the fracture coatings. If no additional deposition or dissolution occurs, $^{234}U/^{238}U$ and $^{230}Th/^{234}U$ will successively move towards secular equilibria. The degree of disequilibrium tends to decrease with depth due to more stagnant conditions /e.g. Suksi 2001, Tullborg et al. 2003/. The redox zone position varies due to short and long term variations in groundwater conditions (e.g. annual variations in groundwater chemistry and land uplift, respectively). Therefore, deposition and removal of U from fluids with different redox conditions may have occurred at a specific depth during very long time.

Since the U content commonly is low in the fracture coatings, analysis of the entire filling is preferred, and may therefore include U both from stable minerals (mostly not reactive) and the mobile phase (mainly adsorbed) dominantly present on goethite and clay minerals. U-series measurements on fracture coatings from crystalline rocks have earlier been studied at the adjacent Äspö subarea /Tullborg et al. 2003/, but also in other areas /Smellie et al. 1986, Gascoyne and Cramer 1987, Griffault et al. 1993, MacKenzie et al. 1992, Suksi and Rasilainen 2002/. Controlling documents for the performance of the activity are listed in Table 1-1. The original results are stored in the primary data base (SICADA) and are traceable by the activity plan number AP PS 400-06-059.

Table 1-1. Controlling documents for the performance of the activity

Activity plan	Number	Version
Sprickmineralogiska undersökningar I KLX09, KLX11A och KLX12A	AP PS 400-06-059	1.0
Method descriptions	**Number**	**Version**
Sprickmineralanalys	SKB MD 144.001	1.0

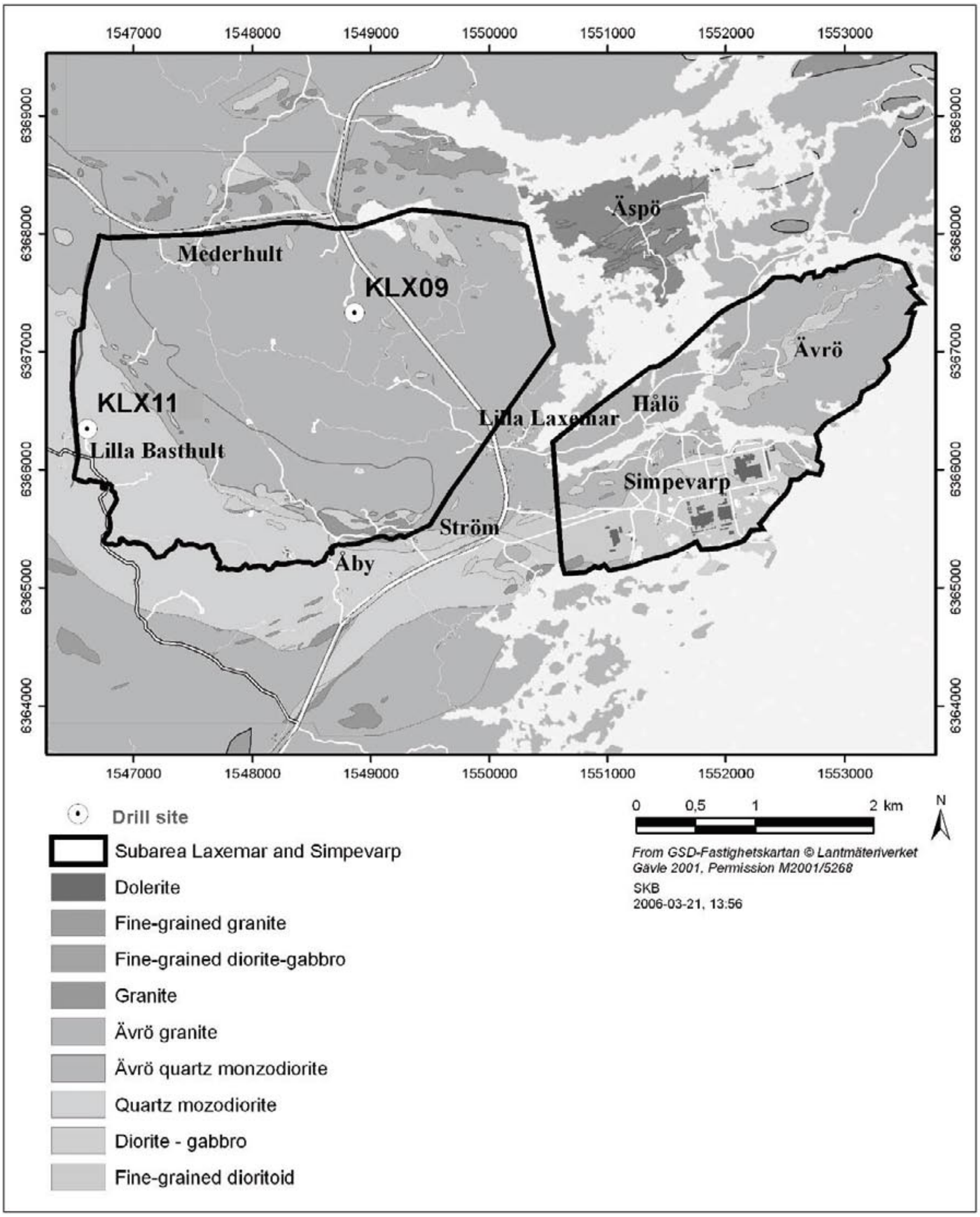

***Figure 1-1.** Geological map showing the surface-location of the drill sites (KLX09 and KLX11) in the Laxemar subarea in the site investigation area at Oskarshamn.*

2 Objective and scope

The aim of this study is to obtain a detailed description of the position, as well as time constraints, of the near surface, recent redox front in the crystalline rock at the Laxemar subarea.

3 Setting

The bedrock in the Laxemar-Simpevarp area is dominated by c. 1.80 Ga diorite to granite /Wahlgren et al. 2006/. The two dominant rock types in the area are "Ävrö granite" (generally granite to quartz monzodiorite) and "Quartz monzodiorite". They have overlapping compositions and are mainly distinguished by texture /Wahlgren et al. 2006/. The rocks within the Laxemar subarea are structurally well preserved, although low-grade metamorphism, discrete foliation and some local shear zones occur. Intrusion of two nearby granites, Götemar and Uthammar (c. 1.45–1.44 Ga /Åhäll 2001/), affected the area with opening of new fractures with associated wall rock alteration, and re-activation of shear zones /Drake et al. 2007, in press/. The Sveconorwegian orogeny affected western Sweden at 0.9–1.1 Ga /e.g. Bingen et al. 2006/, succeeded by development of a foreland basin with sediments covering eastern Sweden /Larson et al. 1999/. After erosion of these sediments in the late Proterozoic the sub-Cambrian peneplain was created /Lidmar-Bergström 1996/ and the presently exposed bedrock surface largely corresponds to this erosion surface. Cambrian to Early Silurian transgression and marine sedimentation resulted in deposition of relatively thin Paleozoic sequences (less than 500 m) and remnants of these are currently found off shore and at a few locations in Sweden /Lindström et al. 1991, Koistinen et al. 2001/. Various thermal indicators, including apatite fission track analyses show that the sedimentary cover had a thickness of several kilometres during the Late Paleozoic /Larson et al. 1999, Cederbom et al. 2000, Cederbom 2001/. These sediments were erosion products from the Scandinavian Caledonides. Subsequent erosion, mainly in the Permian to Triassic, reduced the thickness of the sedimentary cover considerably /Cederbom 2001, Söderlund et al. 2005/. The Cretaceous sea level was about 200 to 300 m higher than at present /Hallam 1984/ and the conditions changed to marine at least in southern Sweden, due to transgressions. Finally, the sedimentary cover was eroded away during uplift in the Tertiary and the present sub-Cambrian surface was re-exposed /Lidmar-Bergström 1996/.

Repeated deformation (e.g. early mylonites and later brittle fractures) have affected the area /Munier and Talbot 1993, Drake and Tullborg 2007/. Most of the fractures and shear zones are older than 1.4 Ga /Drake et al. 2007/ and are commonly associated with intense wall rock alteration, i.e. red-staining, alteration of biotite, plagioclase and magnetite and formation of chlorite, albite, adularia and hematite /Drake et al. 2008/. Although, the red-stained wall rock appears to be oxidised, Mössbauer spectroscopy has revealed that it has similar reducing capacity as the fresh rock /Drake et al. 2008/. Subsequently, these fractures have been repeatedly reactivated at later events (e.g. related to the Sveconorwegian and Caledonian orogenies) at successively lower temperatures /Drake et al. 2007/. Many new fractures formed during the Paleozoic /Alm et al. 2005, Drake et al. 2007/ and many of these have probably been water conducting ever since /Drake and Tullborg 2007, Tullborg et al. 2008/. However, the detailed configuration of the flow paths has changed through time and past groundwaters have left precipitates from which the different groundwater regimes now can be traced /Tullborg et al. 1999/. Earlier investigations in the Laxemar-Simpevarp area have shown that precipitation of calcite, pyrite, clay minerals and goethite (near surface) might have occurred as late as in the Quaternary /Tullborg 1997, Drake and Tullborg 2007/.

During the Quaternary several glaciations influenced the Laxemar-Simpevarp area. The ice sculptured the bedrock surface and removed weathered surface layers. During the end of the latest deglaciation (Weichselian) till was deposited on the relatively flat bedrock surface. The Laxemar subarea is situated below the highest shoreline (at c.100 m.a.s.l.) and the till has been re-worked by wave washing and has been covered by alternating fresh and brackish water sediments during the different stages of the Baltic Sea evolution, the Baltic Ice Lake (–11,500 BP), Yoldia Sea (11,500–10,800 BP), Ancylus Lake (10,800–9,500 BP), the Littorina Sea (9,500 to present, salinity max at 6,500 to 5,000 BP), and similar salinities as at present the last 2 ka, /Westman et al. 1999 and references therein, SKB 2006/. Till and sediment layers were then successively washed away except in areas of low topography. Shortly after the ice withdrawal, the water level regressed abruptly to the level of about 30 m a.s.l. Thereafter, the water level slowly regressed (except for transgression during the Littorina period causing the maximum in salinity mentioned above). The present land upheaval is ~1 mm/year. Because of the slow regression, most of the Laxemar subarea has been land during thousands of years and the investigated drill sites have been above the sea level for at least 10.7 ka /Söderbäck 2008/. In the areas with higher topography (e.g. at the studied drill sites) outcrops are common because the present soil cover was formed recently and is therefore thin. Currently, till and bedrock exposures or areas with a thin soil cover dominate the Laxemar-Simpevarp area /Rudmark et al. 2005/. The appearance of striation directions coinciding with the latest ice progression implies that the last continental ice has scraped the outcrops /Landström et al. 2001, Rudmark et al. 2005/. The present surface is thus the result of mechanical erosion and low-temperature chemical weathering during the Weichselian glaciation and the last post-glacial period /Landström et al. 2001/. The dominance of outcropping rocks in the higher regions implies a rapid transportation of surface water to the lower parts of the area, either by direct runoff or by fracture infiltration. Due to aggressive humic acids, chemical weathering is more intensive below the locally occurring thin soil cover /Landström et al. 2001/.

Because the area is situated close to the Baltic Sea, the hydrogeological/hydrochemical evolution during a glacial cycle involves possible injection of glacial water into the bedrock fractures followed by later marine-brackish conditions, and subsequent interplay between meteoric recharge and glacial rebound, summarised as follows /SKB 2006/:

1. Glacial melt water was, due to high hydraulic heads beneath the ice, in-mixed to considerable depth with non-marine saline water with considerable residence time.
2. Post-glacial Baltic Sea water was later introduced due to density turnover in parts of the Laxemar subarea, especially along valleys.
3. The area rose above the sea-level and meteoric water was recharged and in-mixed with the Baltic Sea- and glacial-brine mixed waters.

A combination of meteoric-brackish sea water and glacial melt water, and old, non-marine, saline waters (brine type waters) is found at varying depths at the site /SKB 2006/.

4 The drill sites and the boreholes

The examined, ~100 m deep, boreholes (KLX09B,C,D,E,F,G and KLX11B,C,D,E,F,) from drill sites KLX09 and KLX11 (Figures 4-1 and 4-2) are characterised by exposed bedrocks or less than 0.5 m of Quaternary deposits /Rudmark et al. 2005/. The bedrock surface was generally exposed at the starting point of each borehole, although about 30–40 cm deep soil pockets were present at the starting point of some boreholes and this soil was removed before drilling. The drilling was carried out by triple-tube technique /e.g. Ask 2007b/ which provides high drill core quality and good preservation of minerals in open fractures. The boreholes are 100–120 m in length (except 152 m in KLX09F) and the drill core diameter is about 50 mm.

For both of the drill sites (KLX09 and KLX11) the boreholes C–F were drilled with a dip of 60° from the horizontal plane and emplaced in a box-like geometry around the centrally located, vertical borehole B (Figures 4-1 and 4-2). On drill site KLX09 an additional borehole (G) was drilled to the east (dip: 60°, starting point c. 50 m east of KLX09D). Drill site KLX09 is located closer to the Baltic Sea, and at a couple of meters lower altitude (starting point of the boreholes: 19.63–23.75 m) than drill site KLX11 (22.65–27.27 m). The KLX09-drill site and boreholes are dominated by Ävrö granite, with occasional 5 m sections of mafic rock in some boreholes /Forssberg et al. 2005, Ask 2007ab/. The KLX11-drill site and boreholes are dominated by quartz monzodiorite, with some exceptions, e.g. Ävrö granite in KLX11D:0–50 m /Ask 2006, Cronquist et al. 2006/.

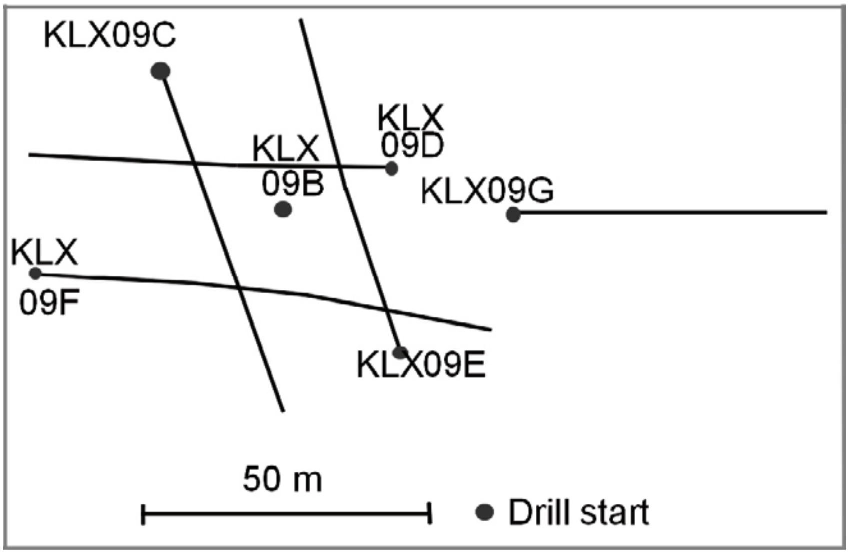

Figure 4-1. *Map of the projections of boreholes KLX09B-G.*

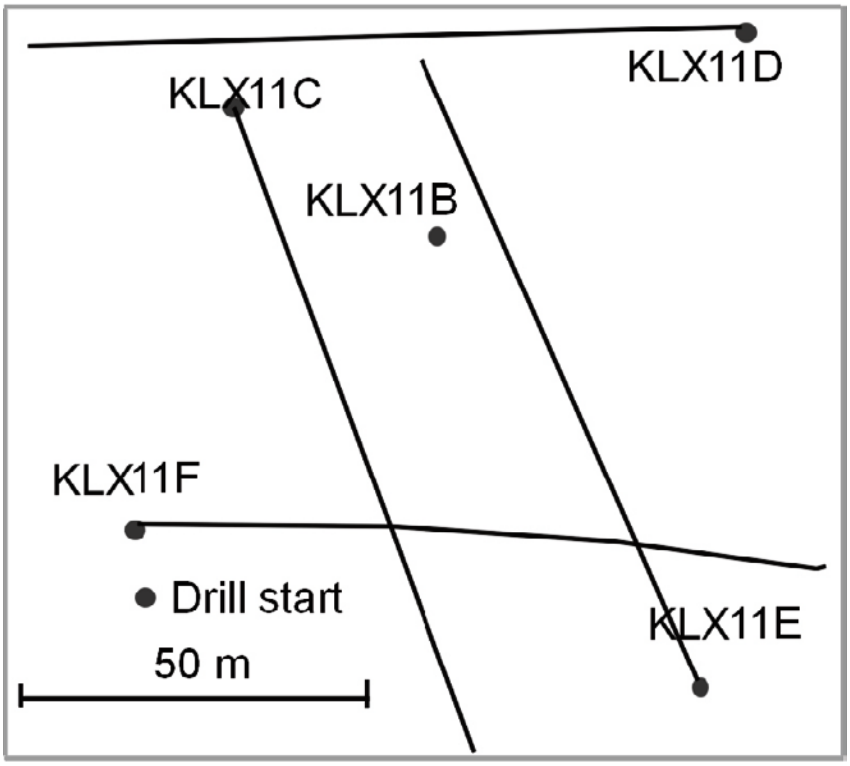

Figure 4-2. *Map of the projections of boreholes KLX11B-F.*

5 Equipment

The following equipment was used in the fracture mineralogy investigations.

- Scanning electron microscope (Hitachi S-3400N) with EDS (Oxford Instruments).
- Microscopes (Leica DMRXP and Leica DMLP).
- Stereo microscope (Leica MZ12).
- Microscope camera (JVC TK-1280E).
- Digital camera (Canon IS-3).
- Rock saw.
- Rock Labs swing mill.
- Knife.
- Magnifying lens – 10x.
- Scanner (Epson 3200) and Polaroid filters.
- Computer software, e.g. Corel Draw 11, WellCad, BIPS, Link ISIS.
- Stable carbon and oxygen isotope analysis equipment.

All of the equipment mentioned above is the property of the Department of Earth Sciences, University of Gothenburg, SKB or the authors.

External laboratory equipment was used for:

- $^{87}Sr/^{86}Sr$-isotope analyses.
- Sulphur isotope analyses.
- U-series analyses.
- X-ray diffraction analyses.

See chapter 6 for more details.

6 Execution

In total 109 samples were collected from the drill cores from the surface down to 115 m vertical depth (Table 6-1). The sampling was focused on open fractures with large amounts of fracture coating (for complete mineralogical, chemical, and U-series analyses) and/or pyrite and goethite. Most samples were collected from the upper 30 meters of the boreholes and the uppermost occurrences of pyrite (and calcite) in most boreholes were sampled. The samples from below 30 m are generally from shear zones, in contrast to samples above 30 m. Consequently, the samples from below 30 m contain higher amounts of fracture coatings and relatively higher amounts of chlorite and clay minerals. The fracture surface of 70 samples was removed by sawing and investigated using a Hitachi S-3400N scanning electron microscope equipped with an Oxford Instruments energy dispersive system (SEM-EDS) in order to identify minerals and their weathering features. Thereafter, the fracture coating was scraped off using a knife. The scraped off material was then sieved and grains smaller than 0.125 mm was analysed for U-series (22 samples), X-ray diffraction (XRD; 15 samples) and chemistry (35 samples), if the amount was sufficient. Thin sections were prepared from the wall rock and the fracture coating of four near surface fractures in order investigate the weathering and alteration in the wall rock and the fracture coatings, using optical microscope and SEM-EDS.

SEM-EDS analyses were carried out at the Department of Earth Sciences, University of Gothenburg, Sweden. The thin sections were coated with carbon for electron conductivity. The instrument was calibrated at least twice every hour using a cobalt standard linked to simple oxide and mineral standards. The acceleration voltage was 20 kV, the working distance about 10 mm and the specimen current was about 1nA. The investigations were carried out using low vacuum mode (15–20 Pa) for the fracture surface samples. X-ray spectrometric corrections were made by an on-line INCA computer system. Detection limit was 0.1 oxide % and Fe^{2+} and Fe^{3+} were not distinguished. Proper mineral analyses were not achieved for fracture surface samples due to the uneven surface of the samples and minerals from these samples were identified from the spectra or from element ratios.

The XRD analyses were carried out by the Swedish Geological Survey, Uppsala. The samples were divided with a sample separator into one part for major mineral analyses (WR) and one for analysis of the fine fraction (FF). The WR samples were ground in an agate mortar under acetone. The sample powder was randomly orientated in the sample holder (and very small sample volumes on a piece of glass). The FF samples were dispersed in distilled water, filtered and oriented according to /Drever 1973/. Three measurements were carried out on each of the FF samples for clay mineral identification; 1) dried samples 2) saturated with ethyleneglycol for two hours and 3) after heating to 400°C in two hours. Coarser material was wet sieved and dried. The XRD analyses were carried out on a Siemens D5000 theta-theta-diffractometer with Cu-radiation (CuK_α) and graphite monochromator at 40 kV and 40 mA. WR scans were run from 2^o to 65^o (2-theta) without orientation of the samples. FF scans were run from or from 2^o–35^o (2-theta) with step size 0.02^o (2-theta) and counting time 1 s/step. The analyses were performed with a fixed 1^o divergence slit, a 2 mm antiscatter slit and a 0.1 mm receiving slit. Evaluation of the diffractometer raw data were carried out using Bruker AXS DIFFRAC^{PLUS} software (version 2.2), and the programme EVA. The minerals were identified by means of the /PDF 1994/ computer database with additional clay mineral data from /Brindley and Brown 1984, Jasmund and Lagaly 1993/.

The fracture coatings were analysed for major, minor and trace element contents by ALS Analytica AB, Sweden. 0.125 g samples were fused with 0.375 g $LiBO_2$ and dissolved in dilute HNO_3. LOI was not carried out due to the small sample volumes. Concentrations of the elements were determined by ICP-AES and ICP-QMS. Analyses were carried out according to EPA methods (modified) 200.7 (ICP-AES) and 200.8 (ICP-QMS). The accuracy was about 5–10%. The analyses do not distinguish between Fe^{2+} and Fe^{3+} and the total Fe content is given as Fe_2O_3.

The uranium-thorium analyses were carried out at the Scottish Universities Environmental Research Centre, Glasgow. The samples were heated to 600°C (in increments of 100°C if the material was highly organic). The material was washed crucible with H_2O into beaker, 9M HCl was added as well as spike, which was left to equilibrate to room temperature before adding and allow for equilibration within the sample. Aqua regia (1HCl:1HNO_3), H_2O_2 and HF was carried out and digested as required, taking to near dryness for each, except HF where complete dryness is required. Then leaching with 4M HNO_3 was carried out. $Fe(OH)_3$ scavenge using NH_3 was then carried out. The precipitate formed was washed thoroughly and dissolved in the minimum concentration HCl and transferred to a clean beaker. The solution was dried down and taken up in ~50 ml 9M HCl and a di-isopropylether extraction was carried out to remove any Fe. The first (chloride) column was pre-conditioned with ~20 ml of 1.2M HCl and 9M HCl, respectively. Sample was introduced to the column in 9M HCl and the Th fraction collected by washing with (2x25 ml) 9M HCl. The U fraction was eluted with 150 ml 1.2M HCl. The U fraction was taken to dryness and prepared for electrode positioning. The Th fraction was taken to dryness and taken back up in 4M HNO_3 (~50 ml) and an Al precipitation carried out with NH_4OH. Precipitate formed was washed well and dissolved in HNO_3. The solution was then dried down and taken back up in 8M HNO_3 (~50 ml) ready for the second (nitric) column. Second column was pre-conditioned with ~20 ml 1.2M HCl and 8M HNO_3, respectively. Sample was introduced to the column in 8M HNO_3, and rinsed with 2x25 ml aliquots 8M HNO_3. The Th fraction was then eluted with 100 ml 9M HCl and then the Th fraction was taken to dryness and prepared for electrode positioning. Accuracy was better than 5% (at 1σ) for 80% of the analyses and 5–11% for the others.

Analyses of $\delta^{13}C$ and $\delta^{18}O$ in calcite were carried out at Department of Earth Sciences, University of Gothenburg. 150–250 µg samples were roasted in vacuum for 30 minutes at 400°C to remove any organic material or moisture. The samples were then analysed on a VG Prism Series II mass spectrometer with an on-line VG Isocarb preparation system, in which each sample was reacted with 100% phosphoric acid at 90°C for 10 minutes, whereupon the released CO_2 gas was analysed in the mass spectrometer. Results are reported relative to VPDB (accuracy $\delta^{13}C\pm0.05‰$ and $\delta^{18}O\pm0.1‰$, at 2σ, calibrated via NBS-18 and NBS-19).

Analyses of $^{87}Sr/^{86}Sr$ in calcite were carried out at IFE, Norway. Samples of calcite (40–50 mg) were transferred to 2 ml centrifuge tubes, added 200 µl 0.2M HCl, and shaken. The samples were let to react for 10 minutes while shaken in order to release the CO_2 gas. If not completely dissolved another 20 µl 2M HCl was added step-wise until it was dissolved. When the samples were dissolved, the solution was evaporated to dryness. 3 ml of 6M HCl was added to each sample, the lid was put on and the beaker was placed on the hotplate at 90°C overnight. All the samples were centrifuged for about 4 minutes and the liquids transferred to new clean centrifuge tubes. The centrifuge tubes were put on a hotplate at 90°C and evaporated to dryness. The residue was taken up in 200 µl ultrapure 3M HNO_3, centrifuged and loaded onto ion-exchange columns packed with a Sr-Spec crown-ether resin from EIChrom, which retained Sr and allowed most other elements to pass. The Sr-fractions were collected with ultra-pure water, evaporated to dryness and loaded on pre-gassed Re filaments on a turret. The isotopic composition of Sr was determined by thermal ionization mass spectrometry (TIMS) on a Finnigan MAT 261. The $^{87}Sr/^{86}Sr$-ratios are monitored by analysing one NIST/NBS SRM 987 Sr standard, for each turret of 12 samples, and the standard has a recommended $^{87}Sr/^{86}Sr$ value of 0.710248.

Samples of pyrite were analysed for their stable-isotope composition, expressed as $\delta^{34}S$‰ CDT. The crystals were scraped of the fracture surfaces with a knife. Bigger crystals were handpicked from the surface with a pair of tweezers. The analyses were carried out at the Scottish Universities Environmental Research Centre, Glasgow. Sulphur dioxide was liberated from sulphides following the method of /Robinson and Kusakabe 1975/, whereby samples were combusted at 1,070˚C for 25 minutes in the presence of excess Cu_2O. A high temperature furnace containing pure copper ensured that any sulphur trioxide in the combustion products was reduced to SO_2. Sulphur dioxide was separated from excess oxygen and the other combustion products by standard vacuum line techniques, and the purified gas analysed for $^{34}S/^{32}S$ ratio on a dual-inlet Micromass SIRA2 multiple-collector mass spectrometer. Reproducibility of calibrated standards is ± 0.2‰ at one sigma and data are reported in the delta notation relative to V-CDT.

Information of fracture mineral occurrences and fracture frequencies in the boreholes was obtained from the mapping data stored in the SKB database (SICADA). The mapping crew paid extra attention to redox sensitive minerals, e.g. pyrite, goethite, hematite and chlorite as well as calcite. The sampling was carried out with support from the mapping data. The uppermost occurrences of the redox sensitive minerals in each borehole were examined in detail in the present study and the mapping data was updated with these observations.

Table 6-1. Sample types and analyses used for each sample.

Borehole	SecUp (m)	SecLow (m)	X-ray diffraction	SEM-EDS-surface	Chemistry (ICP-AES)	U-series analyses	Thin section	$\delta^{13}C$/ $\delta^{18}O$*	$\delta^{34}S$#	$^{87}Sr/^{86}Sr$*
KLX09B	2.700	2.970					x			
KLX09B	7.180	7.290		x		x				
KLX09B	11.112	11.322		x	x	x				
KLX09B	12.977	13.056		x						
KLX09C	29.738	29.863		x				x		
KLX09C	44.965	45.258		x				x		
KLX09C	47.202	47.383		x				x		
KLX09C	84.999	85.120	x	x	x	x				
KLX09C	85.401	85.532								
KLX09C	117.384	117.545		x			x		x	
KLX09D	0.410	0.510		x			x			
KLX09D	3.700	3.860	x	x	x	x				
KLX09D	7.110	7.340		x				x		
KLX09D	9.460	9.610		x	x					
KLX09D	12.869	13.112		x	x					
KLX09D	19.892	20.003		x				x		
KLX09D	20.204	20.335		x						
KLX09D	23.168	23.441		x				x	x	
KLX09D	29.786	29.917		x				x		x
KLX09D	32.025	32.176		x				x		
KLX09D	83.045	83.180	x	x	x	x				
KLX09D	88.430	88.754	x	x	x	x				
KLX09D	104.592	104.868		x	x	x				
KLX09E	1.005	1.145		x		x				
KLX09E	8.910	9.010		x	x					
KLX09E	11.450	11.650		x	x	x				
KLX09E	25.921	25.951		x						
KLX09E	29.574	29.615		x						
KLX09E	31.959	32.140		x				x		x
KLX09E	33.519	33.564								
KLX09E	71.515	71.916		x				x		
KLX09F	9.900	10.000		x				x		
KLX09F	10.830	10.960		x				x		
KLX09F	12.900	13.060		x	x					
KLX09F	22.600	22.790		x				x		
KLX09F	28.510	28.595		x						
KLX09F	34.180	34.310		x						
KLX09F	42.150	42.420		x						
KLX09F	52.240	52.280		x				x		
KLX09F	54.040	54.160		x				x		

Borehole	SecUp (m)	SecLow (m)	X-ray diffraction	SEM-EDS-surface	Chemistry (ICP-AES)	U-series analyses	Thin section	$\delta^{13}C$/ $\delta^{18}O$*	$\delta^{34}S$#	$^{87}Sr/^{86}Sr$*
KLX09F	58.810	59.050		x	x					
KLX09F	64.540	64.720		x				x		x
KLX09F	68.530	68.720	x	x	x	x				
KLX09F	73.320	73.490								
KLX09F	76.000	76.072		x				x		x
KLX09F	77.770	77.820		x				x		
KLX09F	79.660	79.870	x	x	x	x				
KLX09F	81.780	81.890	x	x	x	x				
KLX09F	93.800	93.990		x						
KLX09F	102.260	102.450		x				x		x
KLX09F	112.810	112.900		x				x		
KLX09F	127.151	127.251								
KLX09F	135.231	135.331		x	x					
KLX09F	144.342	144.532		x						
KLX09G	40.358	40.415		x	x	x		x		
KLX09G	41.168	41.411		x				x	x	
KLX09G	43.055	43.152								
KLX11B	2.080	2.310								
KLX11B	3.480	3.710	x	x	x	x				
KLX11B	5.926	6.010	x	x						
KLX11B	9.135	9.160		x						
KLX11B	10.150	10.320								
KLX11B	13.237	13.500		x	x	x				
KLX11B	76.270	76.395		x				x		
KLX11C	1.590	1.730		x						
KLX11C	5.720	5.980		x				x		
KLX11C	8.372	8.502		x						
KLX11C	13.481	13.591		x	x					
KLX11C	18.450	18.590		x						
KLX11C	37.401	37.481		x						
KLX11C	52.670	52.820					x			
KLX11C	53.580	53.730		x						
KLX11C	58.090	58.180								
KLX11C	69.910	70.199		x			x	x		
KLX11C	80.571	80.741		x						
KLX11C	87.450	87.490		x				x		
KLX11C	93.570	93.770					x			
KLX11D	0.930	1.030		x	x			x		
KLX11D	2.020	2.060		x	x	x				
KLX11D	5.050	5.120		x						
KLX11D	8.010	8.234		x						
KLX11D	13.740	13.805		x				x		
KLX11D	24.250	24.504		x				x		
KLX11D	29.670	30.148		x	x		x			
KLX11D	30.410	30.798					xx	x		
KLX11D	64.336	64.892	x	x	xx	x	x			
KLX11D	96.150	96.290		x				xx		
KLX11D	108.600	108.810			x	x				

Borehole	SecUp (m)	SecLow (m)	X-ray diffraction	SEM-EDS-surface	Chemistry (ICP-AES)	U-series analyses	Thin section	$\delta^{13}C$/ $\delta^{18}O$*	$\delta^{34}S$#	$^{87}Sr/^{86}Sr$*
KLX11E	1.840	1.890			x					
KLX11E	4.405	4.535	x	x	x	x				
KLX11E	19.530	19.972	x	x	x	x				
KLX11E	21.465	21.520		x						
KLX11E	42.345	42.451		x	x	x				
KLX11E	59.870	60.148		x				x		
KLX11E	72.940	73.059								
KLX11E	98.820	98.889		x				x		
KLX11E	109.000	109.114		x			x	x		
KLX11E	113.210	113.379					x			
KLX11E	117.090	117.279		x			x	x	x	
KLX11E	120.830	120.915		x					x	
KLX11F	2.350	2.585		x	x	x	x			
KLX11F	6.631	6.691		x			x			
KLX11F	9.590	9.690		x	x					
KLX11F	15.280	15.485	x	x	x					
KLX11F	17.160	17.430		x						
KLX11F	20.221	20.361		x				x		
KLX11F	52.340	52.570	x	x	x					
KLX11F	70.170	70.430	x	x	x					
KLX11F	111.380	111.490		x						

*Calcite, #Pyrite

7 Results

7.1 Fracture frequencies

The total number of sealed and open fractures per meter is higher in the KLX09B-G-boreholes (generally 7–11 fractures/m) than in the KLX11B-F-boreholes (generally 4–7) and these numbers are relatively constant with depth (all data on fracture frequencies are extracted from the SKB database SICADA). However, the highest number of fractures is found at 70–80 m depth, a depth interval with abundant minor shear zones and crush rock. The open fractures generally make up 30 to 40% of the total number of fractures (deeper sections commonly have c. 15–30% open fractures /Drake et al. 2006/), and there are about 2–3 open fractures/m in the KLX09B-G-boreholes and 1–2 open fractures/m in the KLX11B-F-boreholes. However, in the interval of 70–80 m depth and in the uppermost 10 meters of the boreholes the amount of open fractures per meter is higher (3–4/m in the KLX09B-G-boreholes and 2–3/m in the KLX11B-F- boreholes). The total number of water conducting fractures in each borehole is generally between 37 and 43, except for in KLX11F: 24 and KLX11D: 49 /Sokolnicki and Väisäsvaara 2006, Väisäsvaara et al. 2006, Sokolnicki and Kristiansson 2007/.

7.2 Mineralogy

The fracture coatings consist of a mixture of minerals commonly including chlorite, clay minerals (e.g. illite Figure 7-1i, smectite or mixed layer-clay; corrensite, smectite/illite or vermiculite/smectite), calcite, quartz, K-feldspar, plagioclase, hematite, goethite and pyrite. Accessory minerals include REE-carbonate (probably bastnäsite), barite, zeolites (harmotome and laumontite), chalcopyrite, epidote and an unidentified U-rich silicate. Near the surface, Ce and Mn-oxide (Figure 7-1j) are present in a few samples (although a more precise identification of these minerals was not possible due to the rough surface of the samples and the small size of crystals). SEM-investigations show that chlorite and clay minerals as well as e.g. calcite, hematite, goethite (Figure 7-2), pyrite and REE-carbonate (where present) are generally the outermost minerals of the fracture coating and are thus in contact with the groundwater to a higher degree than e.g. quartz, K-feldspar, epidote and plagioclase. The mineralogy of all the samples is stored in the primary data base (SICADA) and is traceable by the activity plan number 400-06-059. Sample descriptions are listed in Appendix 1.

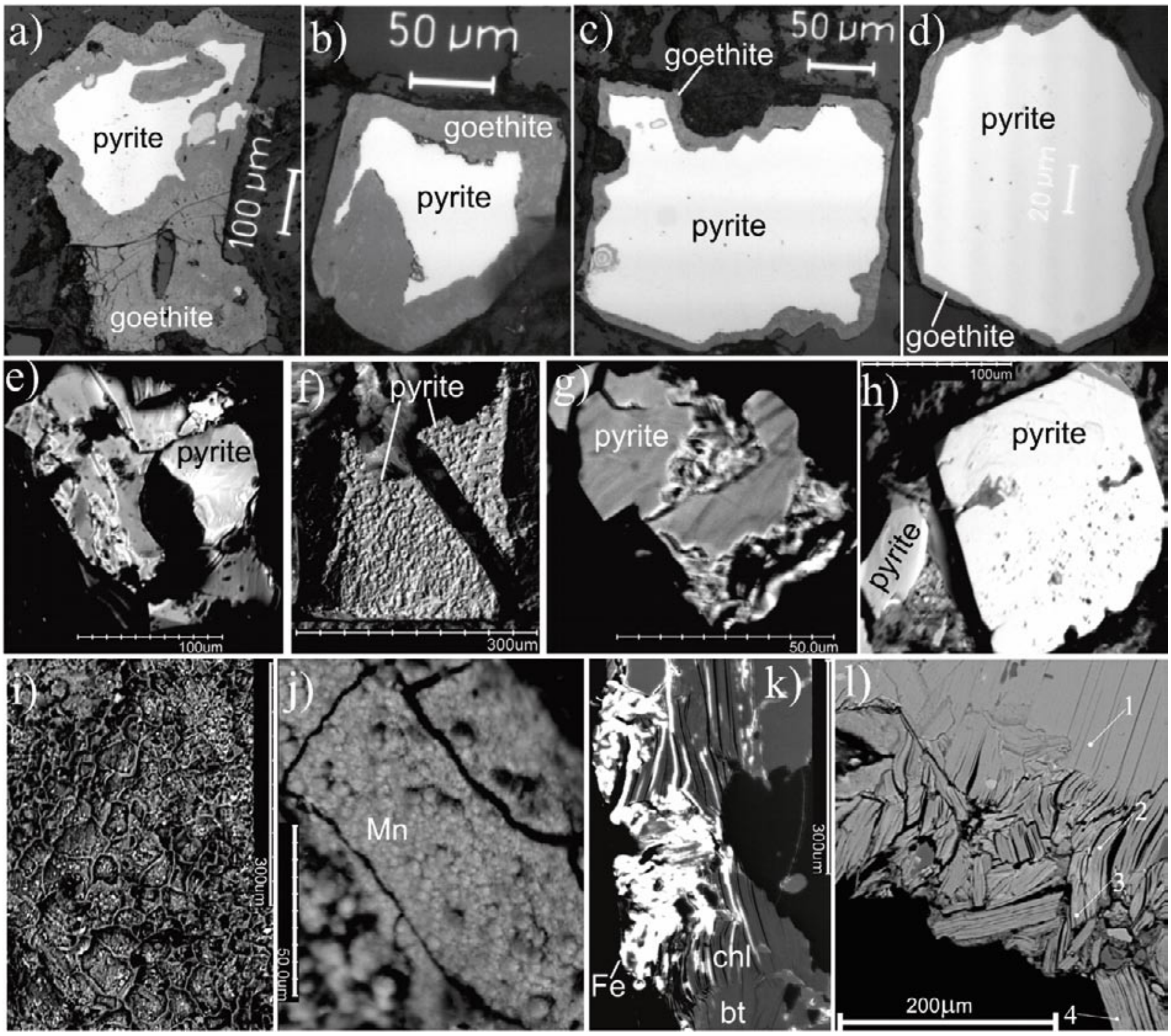

Figure 7-1. *Back-scattered SEM-images. a-d) Wall rock pyrite increasingly replaced by goethite with decreased distance from the fracture (a: 0.4 mm from the fracture, b: 4 mm, c: 10 mm, and d: 17 mm, sample KLX11F: 2.350–2.585 m – thin section). e-g) Altered pyrite crystals on fracture surfaces (e: KLX09B: 11.112–11.322 m, f: KLX09D: 20.204–20.335 m and g: KLX11F: 20.221–20.361 m). h) A rather fresh pyrite crystal (right) and a slightly more altered pyrite crystal (left) on a fracture surface in sample KLX09D: 23.168–23.441 m. i) Illite on a fracture surface (sample KLX09D: 7.110–7.340 m). j) Mn-(oxide or oxyhydroxide) on a fracture surface (KLX09D: 3.700–3.860 m). k) Fe-oxyhydroxide ("Fe") penetrating chlorite ("chl", which has replaced biotite – "bt") close to and at the fracture surface (left side of image, sample KLX11F: 6.631–6.691 m – thin section). l) Fresh biotite (1), replaced by chlorite (2, 3 and 4) close to the fracture surface (EDS analyses of 1-4 are shown in Table 7-1), in sample KLX09D: 0.410–0.510 m (thin section).*

Figure 7-2. *Typical appearance of goethite (brown colour) in a near surface open fracture. Sample KLX11B: 3.480–3.710 m.*

Separation of hematite and goethite (including other FeOOH minerals as well) grown on fracture surfaces is problematic using SEM-EDS because the crystals are very fine-grained and the surface is irregular, which disables proper EDS analysis. In this study goethite is identified by its typical colour (in drill core samples and in thin sections) and by XRD (only diffuse peaks due to low amounts). Because most of the fracture filling hematite in the Laxemar subarea is interpreted (based on paragenesis) to have been formed under conditions different from the present /Drake and Tullborg 2005/, interpretations of recent redox conditions based on Fe^{III}-minerals is mainly based on occurrence of goethite.

According to the mapping of the drill cores the minerals in open fractures are dominated by calcite (present in 76% of the fractures), chlorite (76%), clay minerals (28%), hematite (23%), pyrite (17%), epidote (5.5%) and goethite (3.5%). Mapping data and SEM-EDS investigations reveal that the distribution of the redox sensitive minerals goethite and pyrite as well as calcite varies with depth. The distribution of pyrite and goethite for each borehole is shown in Figures 7-3 (vs. vertical depth) and 7-4 (vs. elevation). Goethite is preferentially found in the upper 10–25 m of the boreholes (differs between the boreholes and is absent near-surface in KLX09G) and occasionally deeper (down to 90 m, often associated with highly transmissive fractures; $> 1 \cdot 10^{-6}$ m^2/s and/or highly fractured sections; > 20 fractures/m). On the contrary, pyrite is absent in the upper 10–25 m (varies between the boreholes, although the uppermost occurrence is commonly at 15–20 m). In most boreholes the near-surface shift from mainly goethite to mainly pyrite in the fractures is distinct, although boreholes KLX09B, KLX09F and KLX11D have alternating goethite and pyrite bearing fractures in the interval 10–25 m. Goethite and pyrite are absent in the interval 10–25 m in KLX09E and this complicates a more precise detection of the redox front location there (chalcopyrite is found at 22 m though). Pyrite crystals in fractures between 10 and 20 m depth is commonly altered and sometimes partially replaced by goethite and clay minerals (Figure 7-1e-h). This alteration decreases in intensity with increased depth and pyrite below 20 m is generally fresh. Pyrite is also observed to be partially or completely replaced by goethite (EDS analyses in Table 7-1) in the wall rock c. 20 mm adjacent to near-surface fractures and this alteration is enhanced towards the fracture (Figure 7-1a-d). Similarly, biotite in the wall rock is replaced by secondary minerals; e.g. chlorite and goethite, which are richer in Fe and OH^- but depleted in Mg, Al, Si and K compared to biotite (Figure 7-1k–l, with EDS analyses in Table 7-1). Penetration of oxygenated fluids into the wall rock adjacent to near-surface fractures is evidenced by red-coloured micro-fractures (filled with goethite, chlorite and/or clay minerals). These have migrated (mainly < 1 cm into the wall rock) along grain boundaries and along the 001-planes within biotite.

The percentage of the total number of open fractures coated with calcite is shown collectively for the KLX09B-G-boreholes and the KLX11B-F-boreholes, respectively in Figure 7-5. Calcite coats 80–95% of the fractures below c. 20–30 m depth but is significantly reduced near-surface (above 20–30 m) to as low as 10–20% in the uppermost 10 meters. The depletion of calcite extends deeper in the KLX11B-F-boreholes (to 30–35 m) than in the KLX09B-G-boreholes (to 20–25 m).

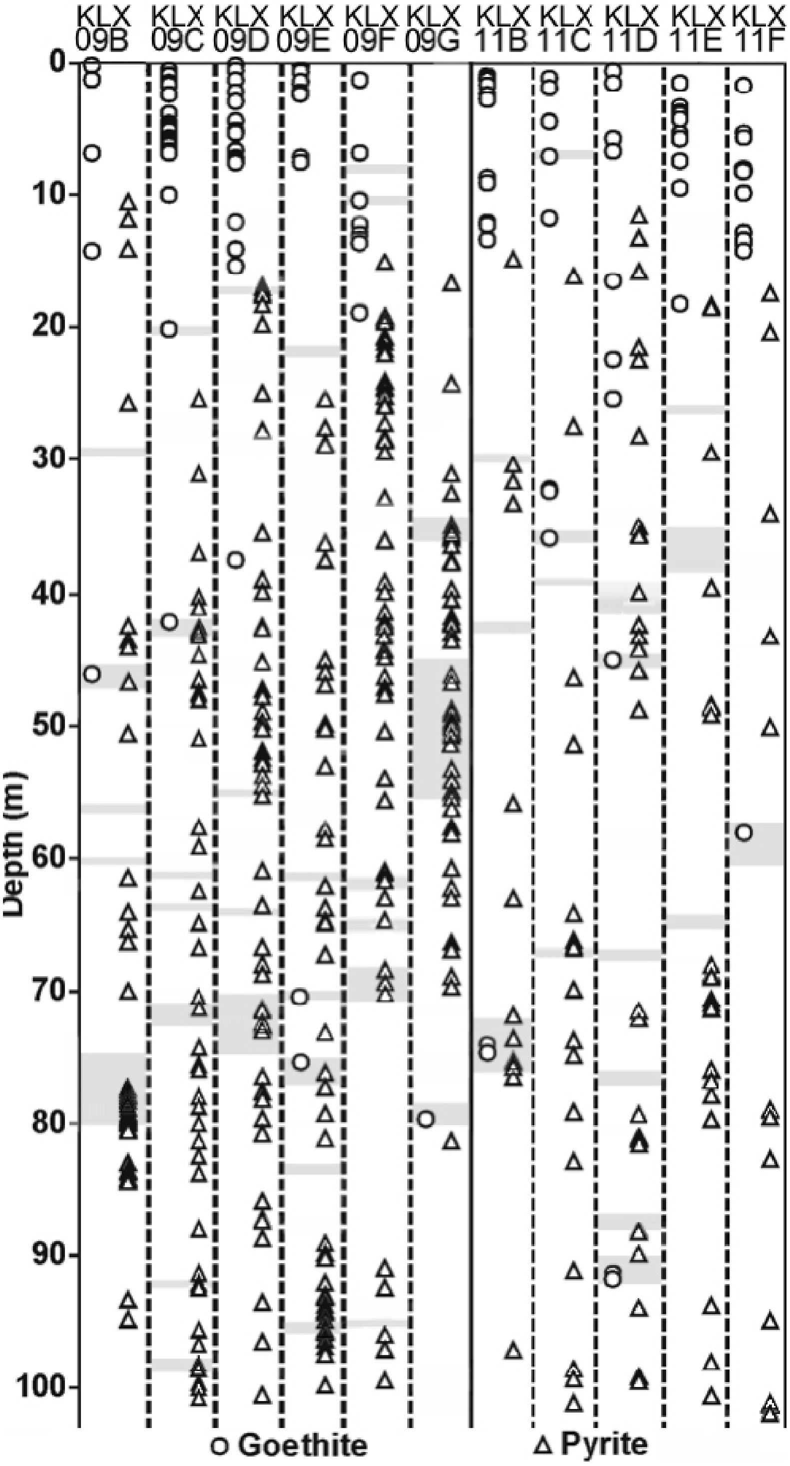

Figure 7-3. *Occurrence of goethite and pyrite in open fractures in KLX09B-G and KLX11B-F shown as vertical depth from the ground surface (each symbol equals one fracture). Shaded areas are intervals with highly transmissive fractures of >1·10^{-6} m^2/s /Sokolnicki and Väisäsvaara 2006, Väisäsvaara et al. 2006, Sokolnicki and Kristiansson 2007/ and/or highly fractured sections (>20 fractures/m). Gravel fill is not shown. Mapping data is from the SKB database SICADA and from this study.*

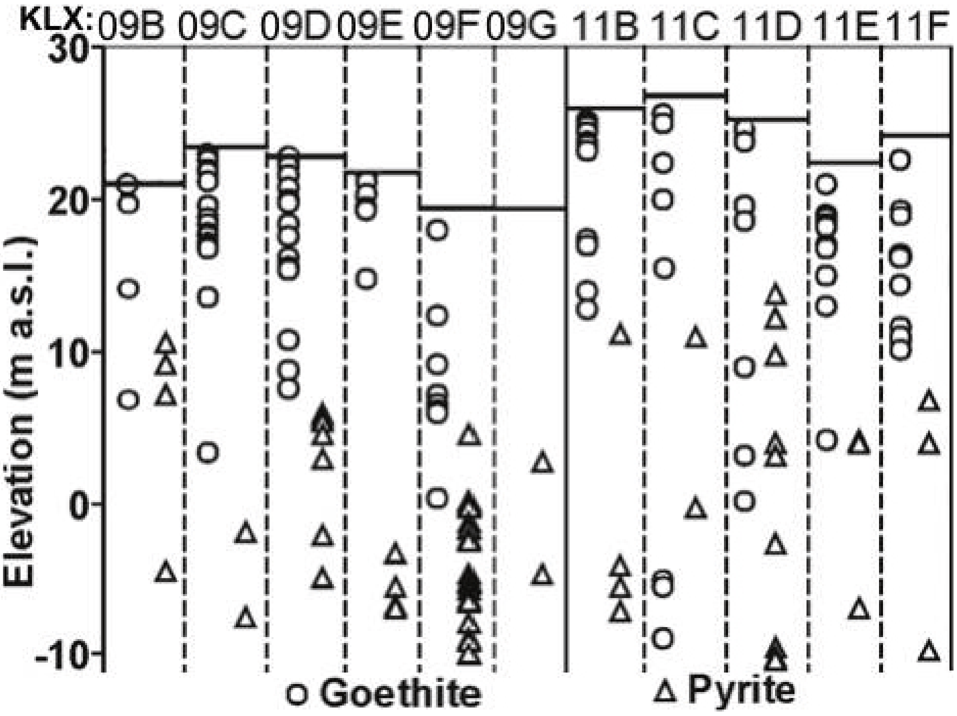

Figure 7-4. *The uppermost occurrences of goethite and pyrite in KLX09B-G (denoted as "09B–09G", for reasons of simplicity) and KLX11B-F (denoted as 11B-F) relative to elevation. Mapping data is from the SKB database SICADA and from this study.*

Table 7-1. SEM-EDS mineral analyses

Fresh and altered (chloritized) biotite; sample KLX09D: 0.15 m (Figure 7-1l)

	MgO	Al_2O_3	SiO_2	K_2O	CaO	TiO_2	MnO	FeO	Total
1	12.6	14.5	36.1	9.3	< 0.1	1.6	0.5	16.7	91.3
2	12.4	14.2	34.5	3.3	0.9	1.4	0.3	18.5	85.5
3	8.6	10.9	21.9	1.2	0.9	0.4	0.2	37.2	81.3
4	8.6	12.0	26.1	3.8	0.7	1.1	0.3	30.6	83.2

Goethite; sample KLX11F: 2.0 m (Figure 7-1a)

	Al_2O_3	SiO_2	CaO	Fe_2O_3	Total
1	1.6	4.3	0.4	82.6	88.9
2	1.6	3.6	0.3	80.0	85.5
3	1.6	4.0	0.4	81.5	87.5
4	1.9	4.2	0.7	79.9	86.7

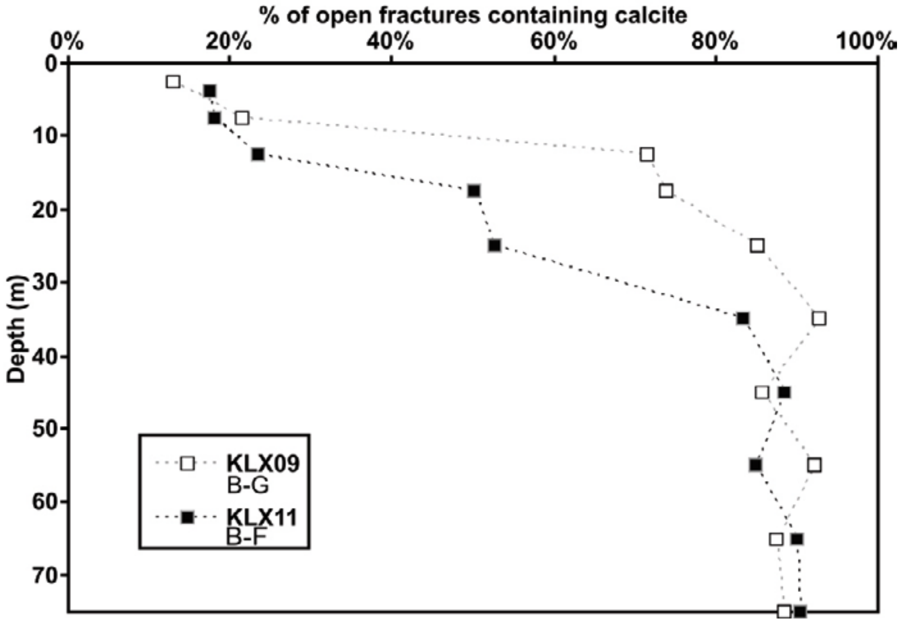

Figure 7-5. Percent of open fractures containing calcite vs. depth for boreholes KLX09B-G and KLX11B-F. The depth intervals are 10 meters (except in the upper 20 meters: 5 m intervals). The trend of 80–95% calcite containing fractures continuous down to 100 m (not included in the graph). No mapping was carried out on the uppermost 2.8 m of the KLX11B-F boreholes and these meters are thus lacking in the graph.

7.3 Chemistry

Most of the analysed fracture fillings (see analyses in Appendix 2) have higher concentrations of e.g. Fe, K, Mg, Mn, Be, Cs and Rb than the wall rock (Ävrö granite and Quartz monzodiorite from outcrops and other boreholes in the Laxemar subarea /Drake et al. 2006/). Approximately 50% of the samples have higher U contents than the wall rock.

A couple of samples, rich in barite and/or harmotome, have significantly higher Ba contents than the wall rock. Most samples have lower contents of Si, Na and Sr than the wall rock. Other elements are mostly within the range of the wall rock chemistry or their deviation is insignificant. Most element concentrations do not show apparent trends with depth (including the redox sensitive Fe). Exceptions are Ca and U which are depleted near surface (and U enriched at great depths), and Mn and the light rare earth elements (LREE), which show elevated concentrations in a number of fracture coating samples near the surface (< 20 m), compared to the deeper samples (> 20 m). Furthermore, Cs concentrations are elevated at depths greater than 50 m and Ba, Co, Cu, P and Ti are partly enriched near the surface. U and Th concentrations are both usually 3 to 10 ppm and U concentrations of above 10 ppm are only found in samples below 11 m depth. Ba, Co, Cu, and P concentrations are mainly within the values of the wall-rock but a minority of the samples shows highly elevated concentrations of these elements (also shown for Ti in one sample) and these are, as a rule, from the upper 20 m. A small number of samples (mostly below 30 m) have much higher Ca concentrations than in the wall-rock, while most fracture coating samples above 10 m have Ca contents that are lower than or similar to the wall-rock, in accordance with the apparent calcite dissolution near the surface, although CaO is related to other phases as well, which makes the depletion in CaO less distinct than the calcite distribution with depth (Figure 7-5). Mn concentrations in the bulk fracture coatings are highly variable near the surface and there is a slight decrease with increasing depth. The most striking feature is the very high Mn contents are found in two fracture coating samples containing Mn-oxide or -oxyhydroxide and Mn-rich clay minerals/chlorite above 10 m depth, indicating the presence of Mn(IV). Most of the fracture coating samples have much higher Cs concentrations than in the wall-rock and the highest concentrations are found in samples below 50 m depth, mainly in clay mineral- (e.g. mixed-layer clay of illite/smectite-type) and chlorite-rich samples. LREE are within the range of the wall-rock for most samples. However, a couple of near surface samples (< 20 m depth) have higher LREE concentrations (La, Ce, Pr, Nd and Sm) than in the wall-rock and these samples contain, possibly Paleozoic, REE-carbonate coatings, rich in Ce, La, Nd and Y /cf. Drake and Tullborg 2005/, and Ce-oxide in one of the samples. In the upper part of the boreholes the La/Yb-ratio in the fracture coatings are occasionally very high (Figure 7-7b). Most samples from 0–20 m depth show positive Ce-anomalies (up to 1.52 Ce_{CN}/ Ce_{CN}*, Figure 7-7b), in contrast to samples from 20–70 m depth, which have slightly negative Ce-anomalies and samples from greater depths than 70 m, which generally lack Ce-anomalies.

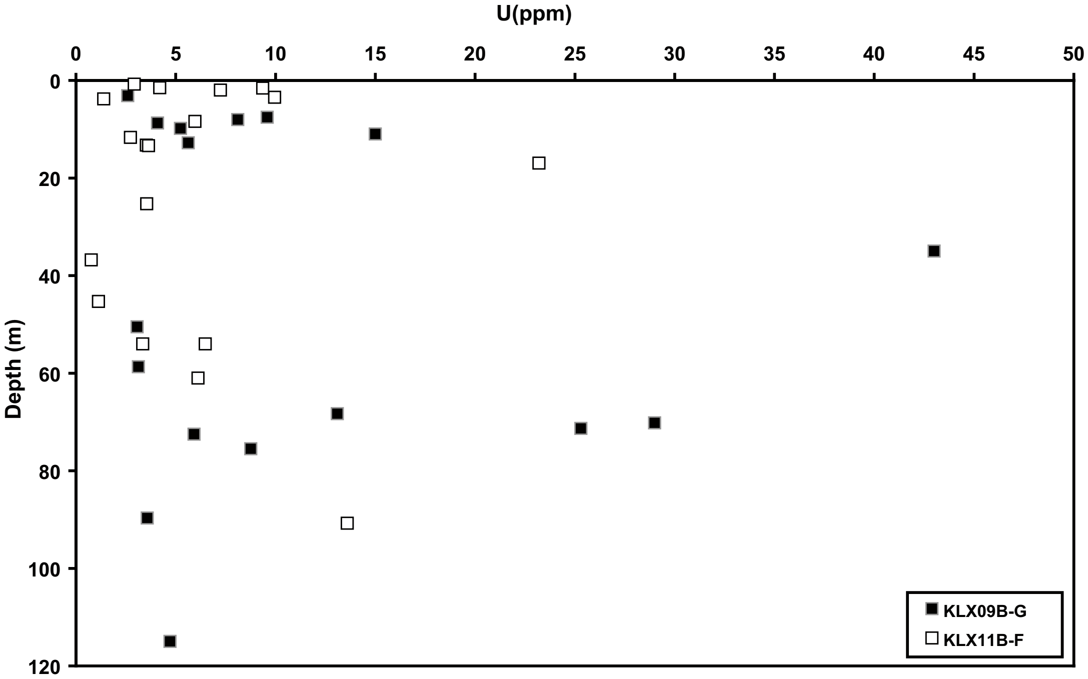

Figure 7-6. *U concentrations vs. depth (vertical) for boreholes KLX09B-G and KLX11B-F.*

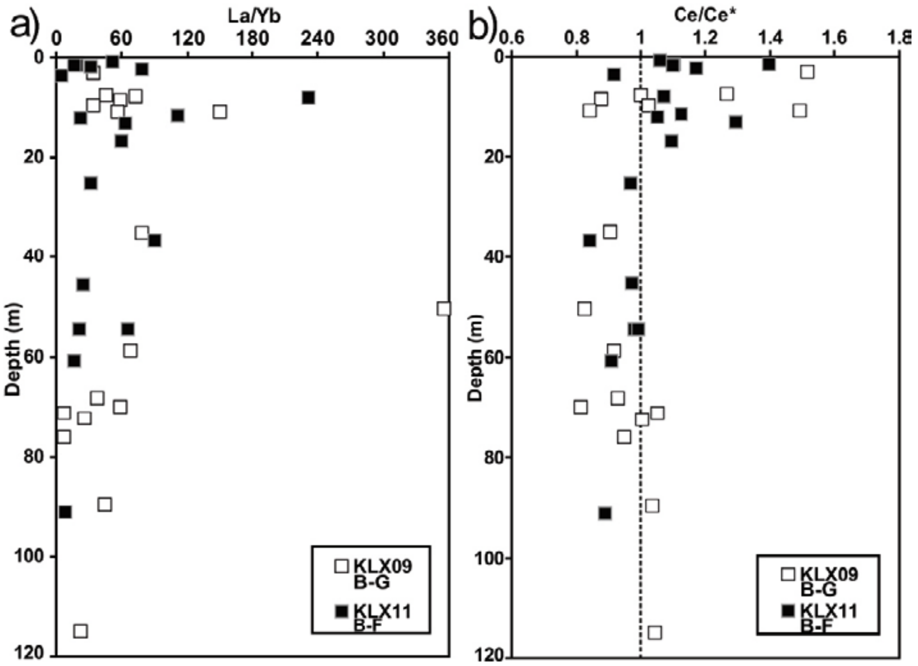

Figure 7-7. *a) La/Yb vs. Depth, b) Ce_{CN}/Ce_{CN}* vs. depth ($Ce_{CN}^* = (La_{CN})^{1/2}(Pr_{CN})^{1/2}$) for samples from boreholes KLX09B-G and KLX11B-F. CN=Chondrite normalised, using chondrite data from /Evansen et al. 1978/.*

7.4 U-series measurements

Results of the uranium decay series analyses are presented in Appendix 3 and in Figures 7-8 and 7-9 (for comparison, 1 Bq/kg is equivalent to a uranium concentration of 0.0810 mg/kg). Comparison of the U and Th values shows reasonable agreement between the isotope dilution alpha spectroscopy and ICP results, suggesting that sample heterogeneity is negligible compared with other uncertainties /cf. MacKenzie et al. 1986/. U activities are generally lower in samples from the upper 15 m than in samples from greater depths. The samples with ^{238}U activities above 240 Bq/kg from depths greater than 35 m are from highly transmissive fractures. The ^{234}U/^{238}U- and ^{230}Th/^{234}U activity ratios (AR) deviates from radioactive secular equilibrium in most of the samples (Figure 7-8). The general trends for ^{230}Th/^{234}U AR and ^{234}U/^{238}U AR with depth are:

- ^{230}Th/^{234}U AR decreases with depth; > 1 above 20 m (median: 1.21, range is 0.96 to 2.01) and < 1 but close to unity at 55–80 m (median: 0.96) and close to unity below 80 m (median 1.06, note that N=2). At 35–55 m the AR varies widely (three samples with AR: 0.82, 1.48 and 2.23).
- Slight excess of ^{234}U (^{234}U/^{238}U AR > 1) is measured at most depths and the AR for samples above 20 m are generally somewhat lower (median: 1.08) than samples from below 20 m; 35–55 m: median 1.25; 55–80 m: median 1.21 and below 80 m: median 1.16 (N=2)).
- Two of the fracture coating samples in the depth interval 35–55 m (KLX11D: 54.5 m and KLX11E: 36.7 m) have excess ^{230}Th and are from fractures currently flowing at rates of $5 \cdot 10^{-7}$ and $1 \cdot 10^{-6}$ m^2/s.

The samples showing the largest disequilibrium ^{230}Th/^{234}U AR (> 1.5) are generally low in ^{238}U.

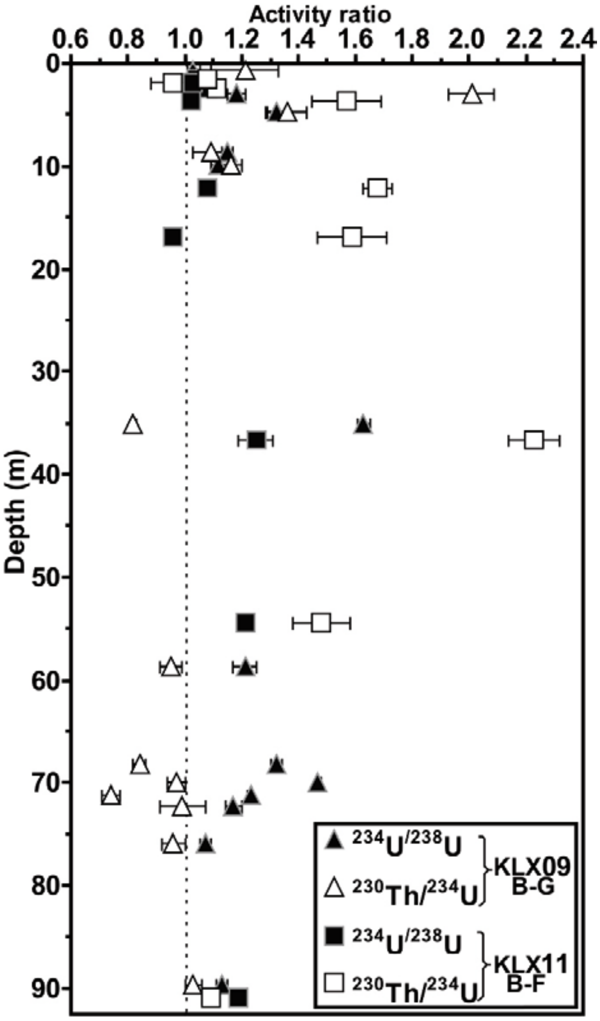

Figure 7-8. *Activity ratios of ^{234}U/^{238}U and ^{230}Th/^{234}U (with errors) vs. depth for fracture coating samples from KLX09B-G and KLX11B-F.*

The ^{238}U, ^{234}U and ^{230}Th data are summarised in a Thiel plot /Thiel et al. 1983/ in Figure 7-9. The result of bulk dissolution of uranium from a system, initially in secular equilibrium, would be to generate a distribution of samples with constant $^{234}U/^{238}U=1$ and $^{230}Th/^{238}U > 1$. Some of the near surface samples plot in positions that could be interpreted as indicating such uranium dissolution, consistent with oxidising conditions at these depths. Importantly, none of the deep samples plot in the uranium-removal sector in Figure 7-9, consistent with maintenance of reducing conditions at depth in the cores over a time period of the order of the ^{230}Th half life of 7.54×10^4 years. The samples with high uranium content and all but one of the other samples from depths greater than 60 m all plot in positions indicating previous deposition of uranium followed by a return towards equilibrium over a time of the order of the ^{230}Th half life.

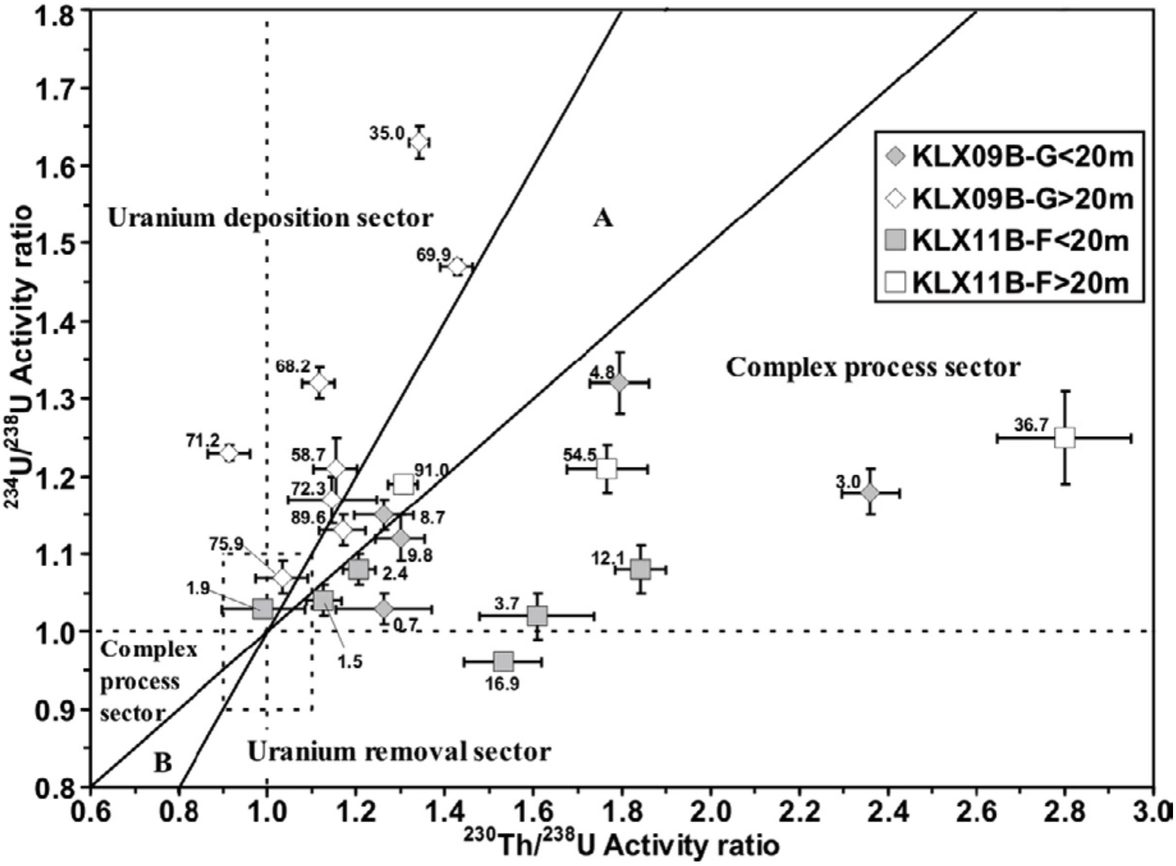

Figure 7-9. *Thiel diagram of uranium decay series for samples from KLX09B-G and KLX11B-F, separated by depths (after /Thiel et al. 1983/). A and B are forbidden sections for any single continuous process. Complex process sector is forbidden for any single process.*

7.5 $\delta^{13}C$, $\delta^{18}O$ and $^{87}Sr/^{86}Sr$ in calcite and $\delta^{34}S$ in pyrite

The stable isotope results ($\delta^{13}C$, $\delta^{18}O$ and $\delta^{34}S$) and $^{87}Sr/^{86}Sr$ results are presented in Appendix 4. $\delta^{13}C$ and $\delta^{18}O$ values in calcite are shown versus depth in Figure 7-10.

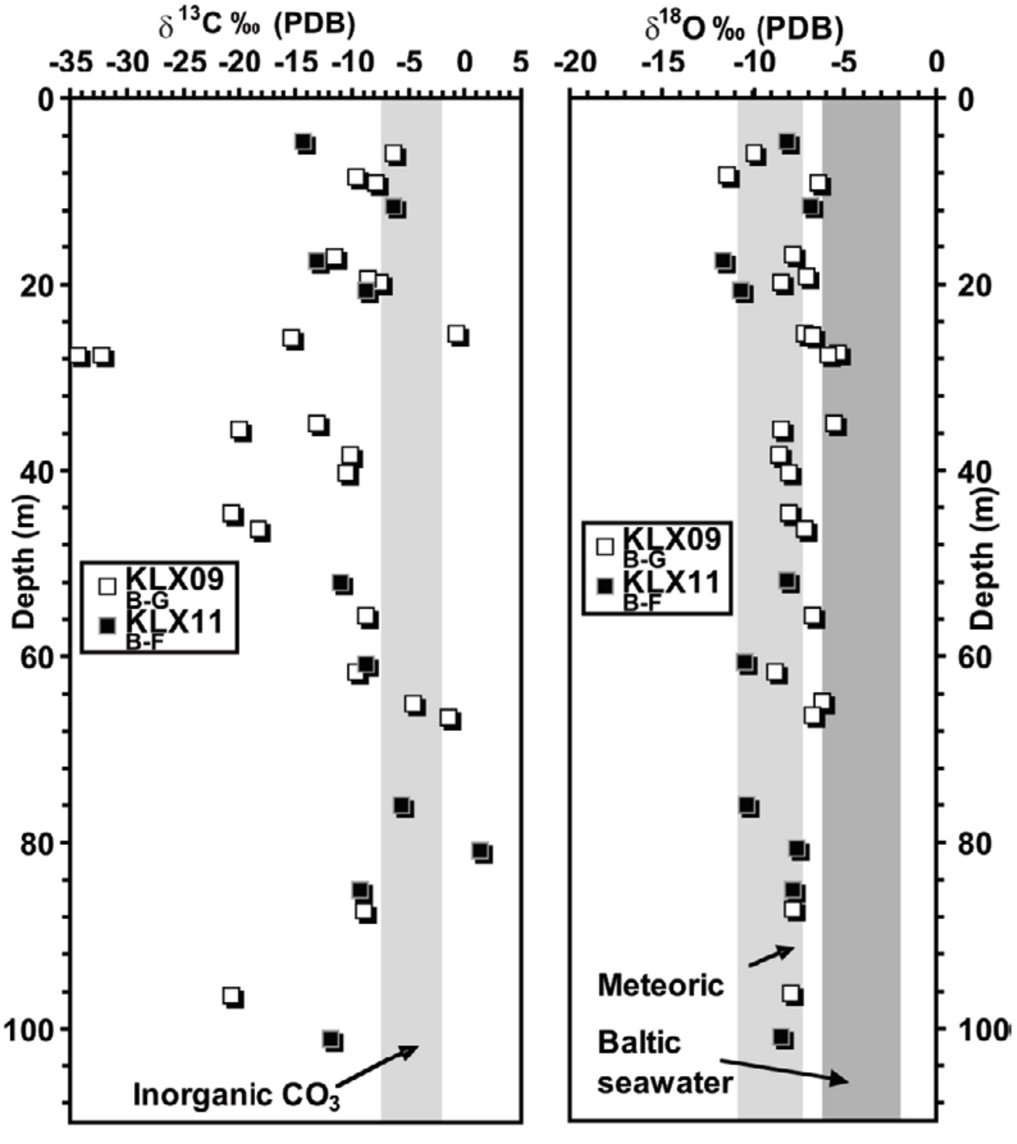

Figure 7-10. Plot of $\delta^{13}C$ and $\delta^{18}O$ values vs. depth for calcite samples from KLX09B-G and KLX11B-F.

8 Discussion

Stable isotope signatures in calcite ($\delta^{13}C$ and $\delta^{18}O$) and in pyrite ($\delta^{34}S$) as well as $^{87}Sr/^{86}Sr$-ratios in calcite from open fractures show that these minerals may have been formed from water in equilibrium with the present groundwater or water with similar signatures as that present (meteoric and/or Baltic seawater with organic and microbial influence). The isotope characteristics are distinctly different from those of Precambrian calcite and pyrite or of Paleozoic warm brine precipitates. These results indicate that (organic rich) waters have descended to at least 100 m depth and have precipitated calcite at low temperatures.

8.1 Mineralogy

The distribution of the redox sensitive minerals pyrite and goethite in open fractures shows that the redox front is generally located at about 15–20 depth below the surface (minimum 10 m depth, Figure 7-3). In boreholes KLX09C and KLX09E the uppermost pyrite occurrences are found at c. 25 m. Overlapping occurrences of pyrite and goethite at 20–25 m depth in some boreholes may indicate that the redox front has fluctuated at these depths. Above the redox front the wall rock is affected by oxygenated water as shown by replacement of pyrite by goethite and alteration of biotite (Figure 7-1a–d, k–l). This alteration is most common within a distance of the 1 mm from the fracture but may locally extend up to 2 cm into the wall rock, as observed in fracture samples from 2 m depth. Goethite occurrences in deeper sections of the boreholes (down to 90 m) are generally found in highly transmissive sections ($> 1\cdot10^6$ m^2/s) and/or highly fractured sections (> 20 fractures/m). Furthermore, the uppermost occurrences of pyrite (at 10–20 m) is generally partly altered which shows that oxygenated fluids have been present in these fractures and that the redox front position is fluctuating over time and probably annual variation as well as long time changes needs to be considered (Figure 7-1e–h). The redox front position is not closely correlated to the local topography (affecting recharge/discharge, Figure 7-4). Other factors (e.g. fracture frequencies and orientations, soil cover/organic content and differences in reducing capacity of the fracture minerals and the wall rock) may be partly responsible for the variation of the redox front position (in elevation as well as in vertical depth) between the boreholes and the drill sites. Redox fronts in KLX09 boreholes are at slightly deeper relative to KLX11B-F boreholes and are considered a consequence of greater fracture frequencies in KLX09B-G host rock.

A redox front position at 20–35 m is indicated by the calcite distribution (dissolution) in open fractures (Figure 7-5). Other mineralogical indications are the absence of chalcopyrite above the redox front defined by the pyrite distribution (except in one sample) and the observation of Ce and Mn-oxide near the surface.

8.2 Chemistry

The positive Ce-anomalies within the upper 20 m (Figure 7-7b) suggest that Ce^{III} is oxidised to Ce^{IV} and probably scavenged onto goethite and/or Mn-oxide /Landström and Tullborg 1995, Vaniman and Chipera 1996, Bau 1999, Takahashi et al. 2000/. These positive Ce-anomalies are in accordance with strong negative Ce-anomalies measured in near surface groundwater in the area / Rönnback et al. 2008/. The process of creating the positive Ce-anomalies in the fracture coatings starts with near surface weathering which results in dissolution of Ce(III) and the other REE. Two different process of subsequent accumulation of Ce(IV) in the solid phase can be outlined as: 1) The REE are sorbed onto the surface of fracture coating goethite (or Mn-oxide/oxyhydroxide) at which Ce(III) is partly oxidised to Ce(IV). Ce(III) and the other REE are then preferentially desorbed compared to Ce(IV) as suggested by /Bau 1999/. 2) Ce(III) is oxidised to Ce(IV) in the aqueous phase followed by preferred sorption of Ce(IV) compared to the other REE onto e.g. fracture coating goethite, due to the high adsorptive activity of Ce(IV), as shown by /Takahashi et al. 2000/. The depth distribution of the positive Ce-anomalies in analyses of bulk fracture coatings is similar to the distribution of goethite, and is thus in good agreement with the redox front position determined by redox sensitive minerals. As a consequence of the preferential precipitation of Ce(IV) above 20 m, fractures in the interval 20–70 m, where the conditions change to reducing, show slightly negative Ce-anomalies. At depths greater than 70 m this effect is no longer visible. High LREE contents (high La/Yb-ratios, Figure 7-7a) and high Mn contents in the upper 20 meters (decrease with depth) indicate influence of descending organic rich waters and possibly also microbial activity. This is shown in other studies in this area /Landström and Tullborg 1995, Pedersen et al. 1997, Tullborg et al. 1999, Bath et al. 2000, Rönnback et al. 2008/. The elevated U contents in some samples below 11 m (> 15 ppm, down to 71 m, Figure 7-6) might be due to deposition of U, mobilised at or near the surface and transported into the fracture system as mobile U(VI) mostly stabilised as carbonate complexes. At greater depths and reducing conditions this U is deposited either due to reduction and/or due to changes in HCO_3^- concentration. The higher amount of e.g. Fe, Mg, Mn, K, Rb and Cs in the fracture fillings compared to the wall rock is probably partly due to the extensive alteration of biotite in the soil cover and wall rock /cf. Drake et al. 2008/ and that these elements are enriched in chlorite and clay minerals which dominate most of the fracture coatings. The much higher Cs contents (and Cs/K-ratios) in most samples below 50 m than in those above 50 m is probably due to samples from chlorite and clay mineral rich shear zones of relatively high sorption capacities for Cs /Grütter et al. 1986, Landström and Tullborg 1995/. Depletion of Ca near surface is associated with dissolution of calcite at these depths.

8.3 U-series disequilibrium

U-series disequilibrium in most of the samples suggests extensive water-rock interaction at least within the last 300 ka to 1 Ma. However, a low number of samples show AR near secular equilibrium which indicates insignificant water-rock interaction during a long time period.

Only two of the samples show secular equilibrium, indicating negligible water-rock interaction within the last 1 Ma, in these specific fractures. Although there is scatter in the data set, mainly because of the heterogeneity of the fracture system (variation in transmissivity and amount of fracture coating material) some depth related trends of recent U mobilisation can be discerned. Based on $^{234}U/^{238}U$ and $^{230}Th/^{238}U$ AR (cf. the Thiel diagram in Figure 7-9) most of the samples from the upper 20 m in the bedrock indicate a complex pattern of deposition and mobilisation during the last ~300 ka (possibly as a result of both oxidising and reducing conditions). Only two samples are consistent with simple removal of bulk U. Some of the samples originating from levels shallower than 20 m are close to $^{230}Th/^{234}U$ unity and do not contain any goethite, which suggests that these fractures have not been open to oxidising water recently. A majority of the samples from depth greater than 35 m show deposition of U either as one single continuous process or as deposition during several occasions. However, elevated values of both $^{234}U/^{238}U$ and $^{230}Th/^{238}U$ AR in two of the deeper samples indicate that fracture coatings have experienced both deposition and removal of U. Higher degree of bulk dissolution of U, probably from oxidising groundwater circulation, in the upper 20 m is indicated by $^{234}U/^{238}U$ AR close to 1 and $^{230}Th/^{234}U > 1$. Fracture coatings from below 55 m tend to have $^{230}Th/^{234}U < 1$ and $^{234}U/^{238}U > 1$, which is consistent with the concept of long-term deposition rather than removal of U under reducing hydrologic conditions /Landström et al. 1989, Tullborg et al. 2003/. Furthermore, bulk removal of U during oxidising conditions near the surface and redeposition of U at greater depths is also possibly indicated by the somewhat increasing ^{238}U with increased depth, especially in highly transmissive fractures, and by the correspondence between low ^{238}U activities and high $^{230}Th/^{234}U$ AR (> 1.5). Excess of ^{234}U in the deeper samples may be due to preferential leaching of ^{234}U relative to ^{238}U, possibly at shallower depths, due to that ^{234}U is more likely present in the oxidised and more easily leached state of U(VI), relative to ^{238}U /e.g. Suksi and Rasilainen 2002/, and/or because of alpha recoil effects that makes more ^{234}U susceptible to leaching than the site of ^{238}U /e.g. Gascoyne et al. 2002/.

The results indicate that recent U oxidation (within 300 ka) has preferentially taken place in the upper 20 m of the boreholes and locally down to 55 m along fractures with high transmissivity. At depths below 55 m recent (within 1 Ma) U deposition under reducing conditions is evident while more stagnant reducing conditions prevail below 80 m. However, a couple of samples between 55–80 m show $^{230}Th/^{234}U$ ~1, suggesting rather stagnant recent conditions in this interval as well.

8.4 $\delta^{13}C$, $\delta^{18}O$ and $^{87}Sr/^{86}Sr$ in calcite and $\delta^{34}S$ in pyrite

The outermost mineral coatings in the studied fractures may possibly be precipitated recently, i.e. during the Quaternary. Stable isotope signatures in calcite ($\delta^{13}C$ and $\delta^{18}O$) and in pyrite ($\delta^{34}S$) as well as $^{87}Sr/^{86}Sr$-ratios in calcite from open fractures in the KLX09B-G- and KLX11B-F-boreholes show that the potentially recent calcite and pyrite may have been formed from water in equilibrium with the present groundwater or water with similar signatures as the present (meteoric and/or Baltic seawater with organic and microbial influence, Figure 7-10). The isotope characteristics are distinctly different from Precambrian calcite and pyrite /cf. Drake and Tullborg 2007/. The low number of calcite samples analysed for $^{87}Sr/^{86}Sr$-ratios show values within the ratios of the present groundwater sampled in Ävrö granite, quartz monzodiorite or fine-grained dioritoid (c. 0.7149–0.7170 /SKB 2006/). It has earlier been shown that water-rock interaction is the process which mainly determines the $^{87}Sr/^{86}Sr$-ratios in the groundwater and other signatures, e.g. marine are seldom preserved in the groundwater or in calcite /Peterman and Wallin 1999, Wallin and Peterman 1999, Drake and Tullborg 2007/. The very high $\delta^{34}S$ values in pyrite at (up to ~ +47‰) is probably due to closed system bacterial sulphate reduction (Rayleigh distillation) causing disequilibrium /e.g. Ohmoto and Goldhaber 1997/, in accordance with observations from Äspö subarea /Wallin 1992, Pedersen et al. 1997/ and Laxemar subarea /SKB 2006/.

9 Conclusions

A combination of different methods, such as detailed mapping and investigation of redox-sensitive minerals, geochemical analyses (especially redox-sensitive elements) and U-series, of fracture coatings in several closely spaced cored boreholes is an excellent method to detect the redox front in crystalline rocks. The location of the redox front shows at what depths oxygenated groundwater associated with varying Quaternary hydrologic conditions (including subglacial or periglacial environments) was able to reach before oxygen was consumed by fracture mineral~~s~~ reactions and organic redox buffering. These hydraulic conditions have been residing in bedrock fractures in the area, as shown by modelling /e.g. Puigdomenech 2001, and references therein/, groundwater chemistry /SKB 2006/ and by characteristics of the youngest fracture minerals /Drake and Tullborg 2007/. These investigations show that the redox front at two drill sites in the Laxemar area is generally positioned at about 15–20 m depth. The main features of the redox front are shown in Figure 9-1. These are generally shown by a shift from:

1. mainly goethite to mainly pyrite in the fractures,
2. positive Ce-anomalies to slightly negative or insignificant Ce-anomalies,
3. mainly removal of U to mainly deposition of U.

Leaching of calcite in open fractures in the upper 20–30 m further support infiltration of very dilute recharge waters which probably have relatively low pH and may at least partly be loaded with oxygen /SKB 2006/. Scattered goethite occurrences down to c. 80 m and occasional signs of U removal at depths between 35 and 55 m is indicated by ^{230}Th/^{234}U AR > 1 in intervals of high transmissivity that facilitate localised percolation of oxygenated groundwater to depths that otherwise experience reduced conditions. Values of ^{230}Th/^{234}U AR that are near or below 1.0 in the sampled fracture coatings below 55 m depth imply that U was not removed preferentially with respect to Th during the last 300 ka and, therefore, that U was likely present in its insoluble reduced form. Although penetration of glacial waters to great depths has been confirmed in the area /SKB 2006/ this study supports the modelling carried out by /Guimerà et al.1999/ and conclusions drawn by /Gascoyne 1999/ that these glacial waters were not oxidising at repository depth. Instead, oxygen in the recharge water is generally consumed within the upper 20 m (+/– 5 m) and to slightly greater depth in fractures or shear zones with increased transmissivities ($\geq 1\cdot10^{-7}$ m^2/s).

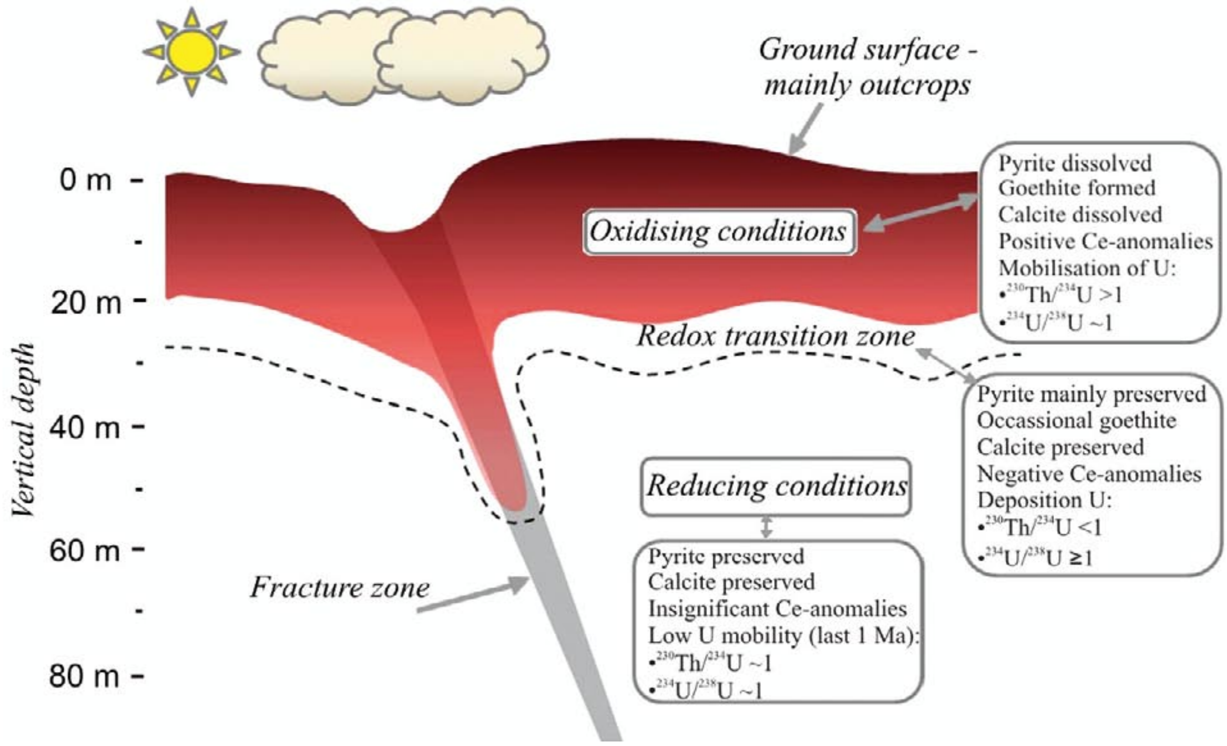

Figure 9-1. *Tentative sketch model of the near-surface redox front in the Laxemar subarea. The different fields represent the depth intervals where mineralogical, chemical and USD analyses of fracture coatings indicate recent oxidising condition, reducing conditions or a transition zone between these.*

10 References

Akagawa F, Yoshida H, Yogo S, Yamomoto K, 2006. Redox front formation in fractured crystalline rock; an analogue of matrix diffusion in an oxidising front along water-conducting fractures. Geochemistry – Exploration, Environment, Analysis, 6, 49–56.

Alm E, Sundblad K, Huhma H, 2005. Sm-Nd isotope determinations of low-temperature fluorite-calcite-galena mineralization in the margins of the Fennoscandian Shield. Swedish Nuclear Fuel and Waste Management Co. Report R-05-66.

Ask H, 2006. Oskarshamn site investigation. Core drilling of short boreholes KLX11B, KLX11C, KLX11D, KLX11E and KLX11F for discrete fracture network investigation (DFN). Swedish Nuclear Fuel and Waste Management Co. Report P-06-283.

Ask H, 2007a. Oskarshamn site investigation. Core drilling of 13 short boreholes (KLX09G, KLX10B, KLX10C, KLX22A, KLX22B, KLX23A, KLX23B, KLX24A, KLX25A, KLX26A, KLX26B, KLX28A and KLX29A) for investigation of minor deformation zones (MDZ). Swedish Nuclear Fuel and Waste Management Co. Report P-06-297.

Ask H, 2007b. Oskarshamn site investigation. Core drilling of short boreholes KLX09B, KLX09C, KLX09D, KLX09E and KLX09F for discrete fracture network investigation (DFN). Swedish Nuclear Fuel and Waste Management Co. Report P-06-265.

Bath A, Milodowski A, Ruotsalainen P, Tullborg E-L, Cortés Ruiz A, Aranyossy J-F, 2000. Evidences from mineralogy and geochemistry for the evolution of groundwater systems during the quaternary for use in radioactive waste repository safety assessment (EQUIP project). EUR report 19613.

Bau M, 1999. Scavenging of dissolved yttrium and rare earths by precipitating iron oxyhydroxide; experimental evidence for Ce oxidation, Y-Ho fractionation, and lanthanide tetrad effect. Geochim. Cosmochim. Acta, 63, 67–77.

Bingen B, Skår O, Marker M, Sigmod E M O, Nordgulen O, Ragnhildstveit J, Mansfeld J, Tucker R D, Liégeois J-P, 2006. Timing of continental building in the Sveconorwegian orogen, SW Scandinavia. Norw. J. Geol., 85, 87–116.

Brindley G W, Brown G eds., 1984. Crystal structures of clay minerals and their X-ray identification, Mineral. Soc. Great Britain and Ireland, Mineral. Soc. Monograph 5.

Cederbom C, 2001. Phanerozoic, pre-Cretaceous thermotectonic events in southern Sweden revealed by fission track thermochronology. Earth Planet. Sc. Lett., 188, 199–209.

Cederbom C, Larson S Å, Tullborg E-L, Stiberg J P, 2000. Fission track thermochronology applied to Phanerozoic thermotectonic events in central and southern Sweden. Tectonophysics, 316, 153–167.

Cronquist T, Forssberg O, Hansen L M, Koyi S, Vestgård J, Wikholm M, 2006. Oskarshamn site investigation. Detailed outcrop mapping on drillsite KLX11. Swedish Nuclear Fuel and Waste Management Co. Report P-06-06.

Dia A, Gruau G, Olivie L G, Riou C, Molenat J, Curmi P, 2000. The distribution of rare earth elements in groundwaters; assessing the role of source-rock composition, redox changes and colloidal particles. Geochim. Cosmochim. Acta, 64, 4131–4151.

Dideriksen K, Christiansen B C, Baker J A, Frandsen C, Balic-Zunic T, Tullborg E-L, Mørup S, Stipp S L S, 2007. Fe-oxide fracture-fillings as a palæo-temperature and -redox indicator: Structure, crystal form, REE content and Fe isotope composition. Chem. Geol., 244, 330–343.

Drake H, Page L, Tullborg E-L, 2007. Oskarshamn site investigation, $^{40}Ar/^{39}Ar$ dating of fracture minerals. Swedish Nuclear Fuel and Waste Management Co. Report P-07-27.

Drake H, Sandström B, Tullborg E-L, 2006. Mineralogy and geochemistry of rocks and fracture fillings from Forsmark and Oskarshamn: Compilation of data for SR-Can. Swedish Nuclear Fuel and Waste Management Co. Report R-06-109.

Drake H, Tullborg E-L, Annersten H, 2008. Red-staining of the wall rock and its influence on the reducing capacity around water conducting fractures. Appl. Geochem. 23. 1898–1920.

Drake H, Tullborg E-L, 2005. Oskarshamn site investigation. Fracture mineralogy and wall rock alteration, results from drill cores KAS04, KA1755A and KLX02. Swedish Nuclear Fuel and Waste Management Co. Report P-05-174.

Drake H, Tullborg E-L, 2007. Paleohydrogeology of the Simpevarp area, southeastern Sweden, as evidenced by stable isotopes in fracture minerals. In: Bullen, T.D, Wang, Y. eds, Water-rock Interaction: Proceedings of the 12th International Symposium on Water-Rock Interaction, Kunming, China, Taylor & Francis, London, pp. 723–726.

Drake H, Tullborg E-L, in press. Paleohydrogeological events recorded by stable isotopes, fluid inclusions and trace elements in fracture minerals in crystalline rock, Simpevarp area, SE Sweden. Applied Geochemistry.

Drever S I, 1973. The preparation of oriented clay mineral specimens for X-ray diffraction analysis by a filter-membrane peel technique. American Mineralogist, 58, 553–554.

Eliasson T, Tullborg E-L, Landström O, 1989. Fracture filling mineralogy and geochemistry at the Swedish HDR research site. In: Baria, R. ed, Camborne School of Mines International Hot Dry rock Conference, Robertson Sc. Publ., London, pp. 425–435.

Evansen N M, Hamilton P J, O'Nions R K, 1978. Rare Earth Abundances in Chondritic Meteorites. Geochim. Cosmochim. Acta, 42, 1199–1212.

Forssberg O, Cronquist T, Hansen L, Vestgård J, 2005. Oskarshamn site investigation. Detailed outcrop mapping at the drill site of KLX09 in Laxemar. Swedish Nuclear Fuel and Waste Management Co. Report P-05-260.

Gascoyne M, 1999. Long-term maintenance of reducing conditions in a spent nuclear fuel repository. A re-examination of critical factors. Swedish Nuclear Fuel and Waste Management Co. Report R-99-41.

Gascoyne M, Cramer J J, 1987. History of actinide and minor element mobility in an Archean granitic batholith in Manitoba, Canada. Appl. Geochem., 2, 37–53.

Gascoyne M, Miller N H, Neymark L A, 2002. Uranium-series disequilibrium in tuffs from Yucca Mountain, Nevada, as evidence of pore-fluid flow over the last million years. Appl. Geochem., 17, 781–792.

Griffault L Y, Gascoyne M, Kamineni C, Kerrich R, Vandergraaf T T, 1993. Actinide and rare earth element characteristics of deep fracture zones in the Lac du Bonnet granitic batholith, Manitoba, Canada. Geochim. Cosmochim. Acta, 57, 1181–1202.

Grütter A, von Gunten H R, Rössler E, 1986. Sorption, desorption, and isotope exchange of cesium (10^{-9}–10^{-3} M) on chlorite. Clay. Clay. Miner., 34, 677–680.

Guimerà J, Duro L, Jordana S, Bruno J, 1999. Effects of ice melting and redox front migration in fractured rocks of low permeability. Swedish Nuclear Fuel and Waste Management Co. Report TR-99-19.

Hallam A, 1984. Pre-Quaternary sea-level changes. Annual Review of Earth and Planetary Sciences, 12, 205.

Jasmund K, Lagaly G eds, 1993. Tonminerale und Tone. D. Steinkopff, Darmstadt.

Koistinen T, Stephens M B, Bogatchev V, Nordgulen Ø, Wennerström M K J eds, 2001. Geological map of the Fennoscandian Shield Scale 1:2 000 000. Geol. Surv. of Finland, Norway and Sweden and Ministry of Natural resources of Russia.

Landström O, Smellie J, Tullborg E-L, 1989. Mineralogical and geochemical studies of fracture-infillings in drillcore KLJ 01, chapter 9. In: Bäckblom, G, Stanfors, R. eds, Interdisciplinary study of post-glacial faulting in the Lansjärv area northern Sweden Swedish Nuclear Fuel and Waste Management Co. Report TR-89-31.

Landström O, Tullborg E-L, 1995. Interactions of trace elements with fracture filling minerals from the Äspö Hard Rock Laboratory. Swedish Nuclear Fuel and Waste Management Co. Report TR-95-13.

Landström O, Tullborg E-L, Eriksson G, Sandell Y, 2001. Effects of glacial/post-glacial weathering compared with hydrothermal alteration – implications for matrix diffusion. Results from drillcore studies in porphyritic quartz monzodiorite from Äspö SE Sweden. Swedish Nuclear Fuel and Waste Management Co. Report R-01-37.

Landström O, Tullborg E-L, 1989. The Influence of Fracture Minerals/Groundwater Interaction on the Mobility of U, Th, REE and other Trace Elements. Swedish Nuclear Fuel and Waste Management Co. Report TR-90-37.

Larson S Å, Tullborg E-L, Cederbom C, Stiberg J P, 1999. Sveconorwegian and Caledonian foreland basins in the Baltic Shield revealed by fission-track thermochronology. Terra Nova, 11, 210–215.

Lidmar-Bergström K, 1996. Long term morphotectonic evolution in Sweden. Geomorphology, 16, 33–59.

Lindström M, Lundqvist J, Lundqvist T, 1991. Sveriges geologi från urtid till nutid. Studentlitteratur, Lund.

MacKenzie A B, Scott R D, Linsalata P, Miekeley N, 1992. Natural decay series studies of the redox front system in the Pocos de Caldas uranium mineralization. J. Geochem. Explor., 17, 289–322.

MacKenzie A B, Scott R D, Smellie J A T, 1986. II: A comparison of neutron activation and alpha spectroscopy analyses of thorium in crystalline rocks. Swedish Nuclear Fuel and Waste Management Co. Report TR-86-01.

Milodowski A E, Tullborg E-L, Buil B, Gomez P, Turrero M-J, Haszeldine S, England G, Gillespie M R, Torres T, Ortiz J E, Zacharias J, Silar J, Chvatal M, Strnad L, Sebek O, Bouch J E, Chenery S R, Chenery C, Shepherd T J, McKervey J A, 2005. Application of Mineralogical, Petrological and Geochemical tools for Evaluating the Palaeohydrogeological Evolution of the PADAMOT Study Sites. PADAMOT Project Technical Report WP2.

Min M, Peng X, Wang J, Osmond J K, 2005. Uranium-series disequilibria as a means to study recent migration of uranium in a sandstone-hosted uranium deposit, NW China. Appl. Radiat. Isotopes, 63, 115–125.

Munier R, Talbot C J, 1993. Segmentation, fragmentation and jostling of cratonic basement in and near Äspo, Southeast Sweden. Tectonics, 12, 713–727.

Ohmoto H, Goldhaber M B, 1997. Sulfur and carbon isotopes, 3rd ed. In: H.L. Barnes (Editor), Geochemistry of hydrothermal ore deposits. John Wiley & Sons, New York, NY, USA.

Osmond J K, Ivanovich M, 1992. Uranium-series mobilization and surface hydrology. In: Ivanovich M, Harmon R S, eds. Uranium-series disequilibrium; application to Earth, marine, and environmental sciences 2nd ed, Oxford Sc. Publ., Oxford.

PDF, 1994. Powder diffraction file computer data base. International Centre for Diffraction Data, Park Lane, USA, Set 1-43.

Pedersen K, Ekendahl S, Tullborg E-L, Furnes H, Thorseth I, Tumyr O, 1997. Evidence of ancient life at 207 m depth in a granitic aquifer. Geology, 25, 827-830.

Peterman Z, Wallin B, 1999. Synopsis of strontium isotope variations in groundwater at Äspö, southern Sweden, Applied Geochemistry, 14, 939–951.

Puigdomenech I, Ambrosi J-P, Eisenlohr L, Lartigue J-E, Banwart S A, Bateman K, Milodowski A E, West J M, Griffault L, Gustafsson E, Hama K, Yoshida H, Kotelnikova S, Pedersen K, Michaud V, Trotignon L, Rivas Perez J, 2001. O_2 depletion in granitic media. The REX project. Swedish Nuclear Fuel and Waste Management Co. Report TR-01-05.

Robinson B W, Kusakabe M, 1975. Quantitative preparation of sulphur dioxide for $^{34}S/^{32}S$ analyses from sulphides by combustion with cuprous oxide. Analytical Chemistry, 47, 1179–1181.

Rudmark L, Malmberg-Persson K, Mikko H, 2005. Oskarshamn site investigation. Investigation of Quaternary deposits 2003–2004. Swedish Nuclear Fuel and Waste Management Co. Report P-05-49.

Rönnback P, Åström M, Gustafsson, J-P, 2008. Comparison of the behaviour of rare earth elements in surface waters, overburden groundwaters and bedrock groundwaters in two granitoidic settings, Eastern Sweden, Appl Geochem. 23, 1862–1880.

SKB, 2004. Hydrogeochemical evaluation for Simpevarp model version 1.2, Preliminary site description of the Simpevarp area. Swedish Nuclear Fuel and Waste Management Co. Report R-04-74.

SKB, 2006. Hydrogeochemical evaluation, Preliminary site description Laxemar subarea – version 1.2. Swedish Nuclear Fuel and Waste Management Co. Report SKB-R-06-12.

Smellie J A T, Mackenzie A B, Scott R D, 1986. An analogue validation study of natural radionuclide migration in crystalline rocks using uranium-series disequilibrium studies. Chem. Geol., 55, 233–254.

Sokolnicki M, Kristiansson S, 2007. Oskarshamn site investigation. Difference flow logging of boreholes KLX11B-F. Subarea Laxemar, Swedish Nuclear Fuel and Waste Management Co. Report P-07-74.

Sokolnicki M, Väisäsvaara J, 2006. Oskarshamn site investigation. Difference flow logging of boreholes KLX09B-F Subarea Laxemar. Swedish Nuclear Fuel and Waste Management Co. Report P-06-199.

Suksi J, 2001. Natural uranium as a tracer in radionuclide geosphere transport studies. PhD-thesis. Report series in Radiochemistry 16/2001, University of Helsinki.

Suksi J, Rasilainen K, 2002. Isotope fractionation of U in rocks reflecting redox conditions around a groundwater flow route. Mat. Res. Soc. Symp., 663, 961–969.

Söderbäck B (Editor), 2008. Geological evolution, palaeoclimate and historic development of the Forsmark and Laxemar/Simpevarp areas, Site descriptive modelling, SDM-Site. Swedish Nuclear Fuel and Waste Management Co. (SKB), Report R-08-19.

Söderlund P, Juez L J, Page L M, Dunai T J, 2005. Extending the time range of apatite (U-Th)/He thermochronometry in slowly cooled terranes; Palaeozoic to Cenozoic exhumation history of southeast Sweden. Earth Planet. Sc. Lett., 239, 266–275.

Takahashi Y, Shimizu H, Kagi H, Yoshida H, Usui A, Nomura M, 2000. A new method for the determination of Ce^{III}/Ce^{IV} ratios in geological materials; application for weathering, sedimentary and diagenetic processes. Earth Planet. Sc. Lett., 182, 201–207.

Thiel K, Vorwerk R, Saager R, Stupp, H D, 1983. ^{235}U fission tracks and ^{238}U-series disequilibria as a means to study recent mobilization of uranium in Archaean pyritic conglomerates. Earth Planet. Sc. Lett., 65, 249–262.

Tullborg E-L, 1997. Recognition of low-temperature processes in the Fennoscandian Shield. PhD Thesis, Göteborg University.

Tullborg E-L, Drake H, Sandström B, 2008. Palaeohydrogeology: A methodology based on fracture mineral studies. Appl. Geochem. 23. 1881–1897.

Tullborg E-L, Landström O, Wallin B, 1999. Low-temperature trace element mobility influenced by microbial activity; indications from fracture calcite and pyrite in crystalline basement. Chem. Geol., 157, 199–218.

Tullborg E-L, Smellie J, Mackenzie A B, 2003. The use of natural uranium decay series studies in support of understanding redox conditions at potential radioactive waste disposal sites. Mat. Res. Soc. Symp., 807, 571–576.

Wahlgren C-H, Hermanson J, Forssberg O, Curtis P, Triumf C-A, Drake H, Tullborg E-L, 2006. Geological description of rock domains and deformation zones in the Simpevarp and Laxemar subareas. Preliminary site description Laxemar subarea – version 1.2. Swedish Nuclear Fuel and Waste Management Co. Report R-05-69.

Wallin B, Peterman Z, 1999. Calcite fracture fillings as indicators of paleohydrology at Laxemar at the Äspö Hard Rock Laboratory, Southern Sweden. Applied Geochemistry, 14, 939–952.

Wallin B, 1992. Sulphur and Oxygen isotope evidence from dissolved sulphates in groundwater and sulphide sulphur in fissure fillings at Äspö, Southeastern Sweden. Svensk Kärnbränslehantering AB, SKB-PR-25-92-08.

Vaniman D T, Chipera S J, 1996. Paleotransport of lanthanides and strontium recorded in calcite compositions from tuffs at Yucca Mountain, Nevada, USA. Geochim. Cosmochim. Acta, 60, 4417–4433.

Westman P, Wastegård S, Schoning K, Gustafsson B, 1999. Salinity change in the Baltic Sea during the last 8,500 years w: evidences causes and models. Swedish Nuclear Fuel and Waste Management Co. Report TR-99-38.

Väisäsvaara J, Leppänen H, Kristiansson S, Pöllänen J, 2006. Oskarshamn site investigation. Difference flow logging of boreholes KLX09G, KLX10B and KLX10C Subarea Laxemar. Swedish Nuclear Fuel and Waste Management Co. Report P-06-229.

Yoshida H, Yamamoto, K., Yogo, S.,Murakami, Y., 2006. An analogue of matrix diffusion enhanced by biogenic redox reaction in fractured sedimentary rock, J. Geochem. Explor., 90, 134–142.

Åhäll K-I, 2001. Åldersbestämning av svårdaterade bergarter i sydöstra Sverige. Swedish Nuclear Fuel and Waste Management Co. Report R-01-60.

Appendix 1

Sample descriptions

Photographs of the samples are shown in this section. Drill core diameter is about 50 mm. The mineralogy of all the samples is stored in the primary data base (SICADA) and is traceable by the activity plan number AP PS 400-06-059. Minerals within brackets are only found in trace amounts.

KLX09B: 2.700–2.970 m

The fracture is coated by quartz, epidote, K-feldspar, chlorite, clay minerals and goethite (thin coating). The fracture surface is rough and the fracture is undulating. The plagioclase alteration and the red-staining increase towards the fracture. Biotite is fresh in most parts of the sample although chloritization (also some mixed-layer clay and probably goethite) is found along the fracture rim. Magnetite is fresh in the whole sample (< 5% hematite). Pyrite is absent.

Photograph of sample KLX09B: 2.700–2.970 m.

KLX09B: 7.180–7.290 m

Minerals: Clay minerals, illite, hematite (or goeethite), K-feldspar, quartz, (U-rich silicate and native Zn)

Photograph of sample KLX09B: 7.180–7.290 m.

KLX09B: 11.112–11.322 m

Minerals: Illite, calcite and harmotome (euhedral),

Photograph of sample KLX09B: 11.112–11.322 m.

KLX09B: 12.977–13.056 m

Minerals: Quartz, epidote, biotite, chalcopyrite, hematite, Fe-rich mixed-layer clay, calcite (thin cover), pyrite and native Zn.

Photograph of sample KLX09B: 12.977–13.056 m (fracture surface).

KLX09C: 29.738–29.863 m

Minerals: Calcite, clay minerals, harmotome, pyrite (sometimes altered, mostly fresh), hematite, quartz and native Zn.

Photograph of sample KLX09C: 29.738–29.863 m.

KLX09C: 44.965–45.258 m

Minerals: Calcite, clay minerals, hematite, REE-carbonate, quartz and epidote.

Photograph of sample KLX09C: 44.965–45.258 m.

KLX09C: 47.202–47.383 m

Minerals: calcite (euhedral), mixed-layer clay, pyrite (cubic, fresh) and hematite.

Photograph of sample KLX09C: 47.202–47.383 m.

KLX09C: 84.999–85.120 m

Minerals: K-feldspar, chlorite, calcite, quartz, illite, plagioclase, hematite, apophyllite, mixed-layer clay and possibly goethite.

Photograph of sample KLX09C: 84.999–85.120 m.

KLX09C: 85.401–85.532 m

Section of crushed rock. Minerals include chlorite and hematite.

Photograph of sample KLX09C: 85.401–85.532 m.

KLX09C: 117.384–117.545 m

Fine-grained whitish filling with coarse-grained wall rock fragments. The filling is bordered by open fractures at both wall rock contacts. The open fractures are coated by quartz, pyrite (cubic, fresh), K-feldspar, illite and calcite. The fine-grained filling consists of quartz, fluorite, calcite and pyrite. Angular wall rock fragments are K-feldspar, plagioclase and quartz. Rounded quartz crystals are also present.

Photograph of sample KLX09C: 117.384–117.545 m.

KLX09D: 0.410–0.510 m

Undulating fracture with rough surface. The fracture surface is covered by plagioclase (wall rock), illite, mixed layer clay, quartz, K-feldspar, chlorite and hematite/Goethite. The wall rock is quite fresh except for the millimetre closest to the fracture, where biotite is altered to chlorite, mixed-layer clay and Goethite (mostly in the rust coloured 0.4 mm zone close to the fracture). The amount of micro-fractures is higher close to the fracture. Magnetite is partly altered to hematite (10 %) in the whole sample. Pyrite is absent. Plagioclase is quite fresh to slightly altered in the whole sample. Goethite and Fe-rich mixed-layer clay are found in micro-fractures (especially along grain boundaries) close to the open fracture (often 0.4 mm into the wall rock but not further than 1 cm).

Photograph of sample KLX09D: 0.410–0.510 m.

KLX09D: 3.700–3.860 m

Minerals: Laumontite, chlorite, plagioclase, calcite, K-feldspar, corrensite, apophyllite, quartz, antigorite, magnetite, Mn-oxide, hematite/goethite, epidote, REE-carbonate (and harmotome).

Photograph of sample KLX09D: 3.700–3.860 m.

KLX09D: 7.110–7.340 m

Minerals: Chlorite, mixed-layer clay, illite, hematite, albite and K-feldspar.

Photograph of sample KLX09D: 7.110–7.340 m.

KLX09D: 9.460–9.610 m

Minerals: Calcite, illite, clay minerals, chlorite, hematite, quartz, K-feldspar, REE-carbonate, (barite and harmotome).

Photograph of sample KLX09D: 9.460–9.610 m.

KLX09D: 12.869–13.112 m

Minerals: K-feldspar, chlorite, clay minerals, illite, hematite and quartz.

Photograph of sample KLX09D: 12.869–13.112 m.

KLX09D: 19.892–20.003 m

Minerals: Calcite, mixed-layer clay (and pyrite).

Photograph of sample KLX09D: 19.892–20.003 m.

KLX09D: 20.204–20.335 m

Minerals: Chlorite (in mixed-layer clay), pyrite (altered to a mineral richer in Fe than pyrite – possibly goethite and chlorite).

Photograph of sample KLX09D: 20.204–20.335 m (fracture surface).

KLX09D: 23.168–23.441 m

Minerals: Harmotome (euhedral), calcite (scalenohedral), mixed-layer clay and pyrite (fresh).

Photograph of sample KLX09D: 23.168–23.441 m.

KLX09D: 29.786–29.917 m

Minerals: Calcite, mixed-layer clay, illite, hematite and apatite.

Photograph of sample KLX09D: 29.786–29.917 m.

KLX09D: 32.025–32.176 m

Minerals: Calcite, illite, mixed-layer clay, quartz, plagioclase, hematite, and pyrite (mostly fresh, sometimes altered).

Photograph of sample KLX09D: 32.025–32.176 m.

KLX09D: 83.045–83.180 m

Minerals: Chlorite, quartz, calcite, illite, K-feldspar, plagioclase and hematite.

Photograph of sample KLX09D: 83.045–83.180 m.

KLX09D: 88.430–88.754 m

Minerals: Quartz, illite, K-feldspar, plagioclase, calcite, chlorite (and hematite).

Photograph of sample KLX09D: 88.430–88.754 m (fracture surface).

KLX09D: 104.592–104.868 m

Minerals: chlorite, illite, quartz, (pyrite and hematite).

Photograph of sample KLX09D: 104.592–104.868 m (fracture surface).

KLX09E: 1.005–1.145 m

Minerals: Illite, chlorite, hematite/goethite, apatite, quartz, kaolinite and K-feldspar.

Photograph of sample KLX09E: 1.005–1.145 m.

KLX09E: 8.910–9.010 m

Minerals: Calcite, clay minerals, illite, K-feldspar, Mn-oxide, hematite/goethite, (barite, native Zn, quartz, REE-carbonate and U-silicate).

Photograph of sample KLX09E: 8.910–9.010 m.

KLX09E: 11.450–11.650 m

Minerals: Calcite, illite, clay minerals, chlorite, quartz, K-feldspar, REE-carbonate and hematite.

Photograph of sample KLX09E: 11.450–11.650 m.

KLX09E: 25.921–25.951 m

Minerals: Illite, mixed-layer clay, fluorite, calcite, U-rich silicate, Ti-Fe oxide, chalcopyrite, native Cu (incl. Sn, Ni, Fe, Co, Mn), hematite, REE-carbonate, goethite and K-feldspar.

Photograph of sample KLX09E: 25.921–25.951 m.

KLX09E: 29.574–29.615 m

Minerals: Calcite, mixed-layer clay, illite, K-feldspar, plagioclase, (REE-carbonate, galena, chalcopyrite [slightly altered] and U-rich silicate).

Photograph of sample KLX09E: 29.574–29.615 m (fracture surface).

KLX09E: 31.959–32.140 m

Minerals: Calcite, illite, mixed-layer clay and hematite.

Photograph of sample KLX09E: 31.959–32.140 m.

KLX09E: 33.519–33.564 m

Open fracture with a fracture mineral coating including minerals chlorite and pyrite.

Photograph of sample KLX09E: 33.519–33.564 m (fracture surface).

KLX09E: 71.515.71.916 m

Minerals: Calcite (mostly without morphology, sometimes scalenohedral), mixed-layer clay, quartz, fluorite (cubic), REE-carbonate, hematite and galena.

Photograph of sample KLX09E: 71.515.71.916 m (fracture surface).

KLX09F: 9.900–10.000 m

Minerals: Calcite, mixed-layer clay, K-feldspar, illite, hematite, (native Zn, REE-carbonate and U-rich silicate).

Photograph of sample KLX09F: 9.900–10.000 m (fracture surface).

KLX09F: 10.830–10.960 m

Minerals: Calcite, mixed-layer clay, illite, chlorite, quartz, K-feldspar, hematite and REE-carbonate.

Photograph of sample KLX09F: 10.830–10.960 m (fracture surface).

KLX09F: 12.900–13.060 m

Minerals: illite, chlorite, clay minerals, albite, hematite, REE-carbonate, barite, epidote and harmotome.

Photograph of sample KLX09F: 12.900–13.060 m.

KLX09F: 22.600–22.790 m

Minerals: Mixed-layer clay, calcite (equant), illite, galena and K-feldspar.

Photograph of sample KLX09F: 22.600–22.790 m (fracture surface).

KLX09F: 28.510–28.595 m

Minerals: Mixed-layer clay, chlorite, illite, K-feldspar, calcite, (hematite, pyrite, U-rich silicate, chalcopyrite, galena and native Zn)

Photograph of sample KLX09F: 28.510–28.595 m.

KLX09F: 34.180–34.310 m

Minerals: Chlorite, mixed-layer clay, illite, fluorite, pyrite (slightly altered), REE-carbonate and galena.

Photograph of sample KLX09F: 34.180–34.310 m.

KLX09F: 42.150–42.420 m

Minerals: Mixed-layer clay, illite, pyrite (cubic, fresh), calcite, harmotome (euhedral), quartz, REE-carbonate, (galena and U-rich silicate).

Photograph of sample KLX09F: 42.150–42.420 m (fracture surface).

KLX09F: 52.240–52.280 m

Minerals: Calcite, mixed-layer clay, quartz, hematite and pyrite (anhedral).

Photograph of sample KLX09F: 52.240–52.280 m.

KLX09F: 54.040–54.160 m

Minerals: Calcite, mixed-layer clay, pyrite (fresh), REE-carbonate, hematite, galena and native Zn.

Photograph of sample KLX09F: 54.040–54.160 m (fracture surface).

KLX09F: 58.810–59.050 m

Minerals: Calcite, chlorite and clay minerals.

Photograph of sample KLX09F: 58.810–59.050 m.

KLX09F: 64.540–64.720 m

Minerals: Calcite, fluorite, mixed-layer clay, barite, REE-carbonate, hematite, pyrite and galena.

Photograph of sample KLX09F: 64.540–64.720 m.

KLX09F: 68.530–68.720 m

Minerals: Calcite, quartz, K-feldspar, plagioclase, chlorite, mixed-layer clay (smectite-dominated, swelling), illite, hematite, and possibly goethite.

Photograph of sample KLX09F: 68.530–68.720 m.

KLX09F: 73.320–73.490 m

Open fracture with a fracture mineral coating including calcite and clay minerals.

Photograph of sample KLX09F: 73.320–73.490 m.

KLX09F: 76.000–76.072 m

Minerals: Calcite.

Photograph of sample KLX09F: 76.000–76.072 m.

KLX09F: 77.770–77.820 m

Minerals: Calcite (nailhead), pyrite (cubic, fresh), Mixed-layer clay, plagioclase and apatite.

Photograph of sample KLX09F: 77.770–77.820 m.

KLX09F: 79.660–79.870 m

Minerals: Quartz, K-feldspar, plagioclase, chlorite, illite, calcite, mixed-layer clay (smectite/illite-dominated, swelling).

Photograph of sample KLX09F: 79.660–79.870 m.

KLX09F: 81.780–81.890 m

Minerals: chlorite, illite, calcite, plagioclase, K-feldspar, quartz and hematite.

Photograph of sample KLX09F: 81.780–81.890 m.

KLX09F: 93.800–93.990 m

Minerals: Illite (platy), calcite, REE-carbonate, (hematite and galena).

Photograph of sample KLX09F: 93.800–93.990 m.

KLX09F: 102.260–102.450 m

Minerals: Calcite, mixed-layer clay, pyrite (cubic, fresh) and apatite (euhedral).

Photograph of sample KLX09F: 102.260–102.450 m.

KLX09F: 112.810–112.900 m

Minerals: Calcite, mixed-layer clay, pyrite (fresh), hematite, plagioclase, (barite [euhedral] and native Zn).

Photograph of sample KLX09F: 112.810–112.900 m.

KLX09F: 127.151–127.251 m

Open fracture with a fracture mineral coating including minerals chlorite and hematite.

Photograph of sample KLX09F: 127.151–127.251 m.

KLX09F: 135.231–135.331 m

Minerals: Chlorite, clay minerals, illite, quartz, hematite and quartz.

Photograph of sample KLX09F: 135.231–135.331 m.

KLX09F: 144.342–144.532 m

Minerals: Mixed-layer clay, illite, pyrite (cubic, fresh), calcite, (and galena).

Photograph of sample KLX09F: 144.342–144.532 m.

KLX09G: 40.358–40.415 m

Minerals: Calcite, clay minerals, illite, hematite, (pyrite, sphalerite and chalcopyrite).

Photograph of sample KLX09G: 40.358–40.415 m.

KLX09G: 41.168–41.411 m

Minerals: Calcite, (scalenohedral), pyrite (cubic, fresh), mixed-layer clay (covers calcite), K-feldspar and hematite.

Photograph of sample KLX09G: 41.168–41.411 m.

KLX09G: 43.055–43.152 m

Open fracture with a fracture mineral coating including clay minerals.

Photograph of sample KLX09G: 43.055–43.152 m.

KLX11B: 2.080–2.310 m

Open fracture with a fracture mineral coating including minerals goethite and clay minerals.

Photograph of sample KLX11B: 2.080–2.310 m.

KLX11B: 3.480–3.710 m

Minerals: Chlorite, clay minerals, illite, hematite/goethite, prehnite, K-feldspar, quartz and calcite.

Photograph of sample KLX11B: 3.480–3.710 m.

KLX11B: 5.926–6.010 m

Minerals: Quartz, chlorite, biotite, K-feldspar, plagioclase, mixed-layer clay (smectite/chlorite-dominated, swelling), illite and barite.

Photograph of sample KLX11B: 5.926–6.010 m.

KLX11B: 9.135–9.160 m

Minerals: Quartz, mixed-layer clay, calcite, REE-carbonate, illite, albite, K-feldspar, native Cu (incl. Pb, Sn, Fe), native Zn, hematite and epidote.

Photograph of sample KLX11B: 9.135–9.160 m.

KLX11B: 10.150–10.320 m

Open fracture with a fracture mineral coating including minerals goethite and clay minerals.

Photograph of sample KLX11B: 10.150–10.320 m.

KLX11B: 13.237–13.500 m

Minerals: Clay minerals, illite, hematite, goethite and K-feldspar.

Photograph of sample KLX11B: 13.237–13.500 m.

KLX11B: 76.270–76.395 m

Minerals: Illite, mixed-layer clay, calcite and REE-carbonate,

Photograph of sample KLX11B: 76.270–76.395 m (fracture surface).

KLX11C: 1.590–1.730 m

Minerals: Illite, mixed-layer clay/chlorite (Fe- and K-rich), quartz, albite, biotite (partly replaced by Fe-rich illite/mixed-layer clay), hematite, (U-rich silicate, W-rich mineral [with Ag, Cu, Fe] and sylvite).

Photograph of sample KLX11C: 1.590–1.730 m.

KLX11C: 5.720–5.980 m

Minerals: Calcite, quartz, hematite, barite and REE-carbonate.

Photograph of sample KLX11C: 5.720–5.980 m.

KLX11C: 8.372–8.502 m

Minerals: Mixed-layer clay (Ca and Fe-rich), quartz, hematite/goethite, Ti-oxide, apatite, plagioclase, (W-rich mineral, Ag-rich mineral and U-rich mineral).

Photograph of sample KLX11C: 8.372–8.502 m.

KLX11C: 13.481–13.591 m

Minerals: Clay minerals, illite, hematite, goethite and K-feldspar.

Photograph of sample KLX11C: 13.481–13.591 m.

KLX11C: 18.450–18.590 m

Minerals: Mixed-layer clay, quartz, REE-carbonate, pyrite (partly altered), hematite, plagioclase (mostly albite) and K-feldspar.

Photograph of sample KLX11C: 18.450–18.590 m (fracture surface with pyrite, chlorite etc).

KLX11C: 37.401–37.481 m

Minerals: Mixed-layer clay, calcite, illite, REE-carbonate, (and barite).

Photograph of sample KLX11C: 37.401–37.481 m.

KLX11C: 52.670–52.820 m

The sandstone filling is about one centimetre wide and is found in an undulating fracture. In the drill core, the sandstone is bordered by open fractures at both of the wall rock contacts. The filling is very fine-grained and greenish in colour and is composed of illite, chlorite, K-feldspar and quartz (low amount of rounded clasts). The filling contains high amounts of wall rock fragments (saussuritized plagioclase, K-feldspar, quartz, chlorite, epidote and biotite). There is possibly a higher amount of fragments (especially coarse-grained) in the centre of the filling.

Photograph of sample KLX11C: 52.670–52.820 m (sandstone-filled fracture).

KLX11C: 53.580–53.730 m

Minerals: Mixed-layer clay, calcite, hematite and pyrite.

Photograph of sample KLX11C: 53.580–53.730 m.

KLX11C: 58.090–58.180 m

Open fracture with a fracture mineral coating including minerals chlorite and clay minerals.

Photograph of sample KLX11C: 58.090–58.180 m.

KLX11C: 69.910–70.199 m

Very fine-grained, greenish filling with high amount of K-feldspar in the matrix. Calcite (and pyrite) is found is coating both of the fracture rims. The filling is made up of few quartz clasts. Fragments are epidote, chlorite, saussuritized plagioclase, and calcite. The wall rock is heavily altered and with a slightly increased red-staining towards the fracture. However, amphibole is not altered in the wall rock. Fresh magnetite and pyrite is found in the wall rock.

The fracture surface of the presently open fracture (along one of the sandstone-wall rock contacts) is covered by calcite (no morphology), illite, mixed layer clay, pyrite (fresh), REE-carbonate, K-feldspar and hematite.

Photograph of sample KLX11C: 69.910–70.199 m (fracture coated by sandstone and nailhead shaped calcite).

KLX11C: 80.571–80.741 m

Minerals: Mixed-layer clay (sometimes Fe-rich), illite, quartz, hematite, (and galena).

Photograph of sample KLX11C: 80.571–80.741 m.

KLX11C: 87.450–87.490 m

Minerals: K-feldspar (bright green, smooth surface), chlorite, mixed-layer clay, calcite, quartz, illite and REE-carbonate.

Photograph of sample KLX11C: 87.450–87.490 m.

KLX11C: 93.570–93.770 m

1.5 centimetre wide sandstone filling. Open fractures are found at both of the wall rock contacts. The filling is greenish in colour, partly very fine-grained, and consists of mostly angular quartz fragments and angular and rounded quartz clasts and subordinate wall rock fragments of plagioclase, K-feldspar (some may be clasts), chlorite and biotite. Clay mineral-rich parts (chlorite, illite, fine-grained quartz and K-feldspar) are found at one of the rims and also extend into the centre of the filling. The fragments are more fine-grained in the clay mineral rich parts compared to the rest of the filling. A thin calcite coating is found at one of the rims. Opaque minerals in the filling are fresh magnetite, magnetite partly replaced by hematite and pyrite.

Photograph of sample KLX11C: 93.570–93.770 m (sandstone-filled fracture).

KLX11D: 0.930–1.030 m

Minerals: Illite, quartz, chlorite, clay minerals, hematite/goethite, K-felsdspar, (W-rich mineral and apatite).

Photograph of sample KLX11D: 0.930–1.030 m (fracture surface with e.g. goethite).

KLX11D: 2.020–2.060 m

Minerals: Chlorite, clay minerals, illite, quartz, K-feldspar, hematite/goethite and plagioclase.

Photograph of sample KLX11D: 2.020–2.060 m (fracture surface with e.g. goethite).

KLX11D: 5.050–5.120 m

Minerals: Illite, K-feldspar, mixed-layer clay/chlorite (Fe-rich), albite, quartz, hematite/goethite, (and native Zn).

Photograph of sample KLX11D: 5.050–5.120 m (fracture surfaces).

KLX11D: 8.010–8.234 m

Minerals: Mixed-layer clay (occasionally very Fe-rich), illite, chlorite, K-feldspar, quartz, hematite (and/or goethite), apatite, (and REE-carbonate)

Photograph of sample KLX11D: 8.010–8.234 m (fracture surfaces).

KLX11D: 13.740–13.805 m

Minerals: Calcite, mixed-layer clay, illite, REE-carbonate, pyrite (rather fresh), harmotome, hematite, fluorite (cubic), (sphalerite, native Zn and barite).

Photograph of sample KLX11D: 13.740–13.805 m (fracture surface with e.g. chlorite and calcite).

KLX11D: 24.250–24.504 m

Minerals: K-feldspar, quartz, albite, calcite and hematite.

Photograph of sample KLX11D: 24.250–24.504 m (fracture surfaces with e.g. chlorite and calcite).

KLX11D: 29.670–30.148 m

The sandstone filling (1–2 cm wide) is found in an undulating fracture which runs parallel to the drill core for about half a meter. In half of the sample an open fracture is found at one of the wall rock-sandstone contacts. The contact between the sandstone and the wall rock is occasionally quite diffuse. The sandstone is made up of rounded clasts of quartz and subordinate less rounded K-feldspar crystals. The amount of matrix (fine-grained quartz, K-feldspar, chlorite and illite) between the clasts is enhanced towards the wall rock contacts. Coarse-grained fragments from the wall rock are found within the filling. Calcite is found in a fracture along one of the wall rock-sandstone contacts. The calcite have also entered the sandstone as cement from this fracture which indicate that the calcite filling is formed subsequently to the sandstone emplacement.

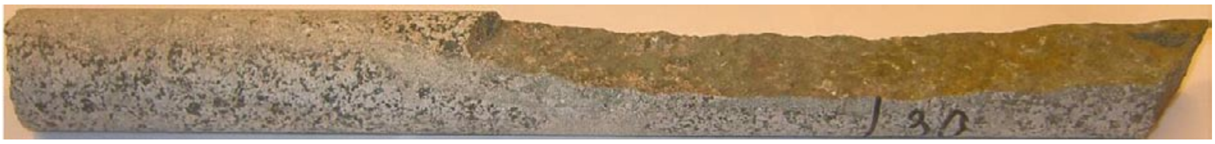

Photograph of sample KLX11D: 29.670–30.148 m (sandstone filled fracture, chlorite, goethite coat the open fracture).

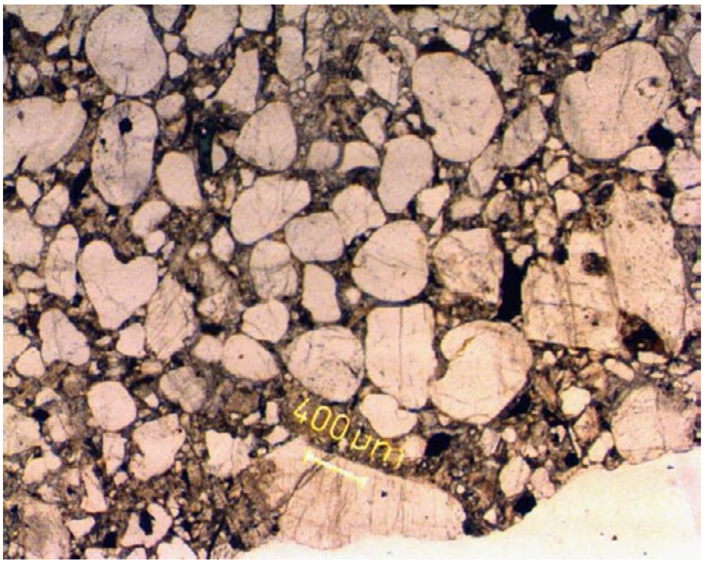

KLX11D: 29.670–30.148 m (photomicrograph of sandstone).

KLX11D: 30.410–30.798 m

Thin section 1:
The sandstone filling (1–2 cm wide) is found in an undulating fracture which runs parallel to the drill cored for about half a meter. Thin apophyses of the major sandstone fracture into the wall rock are observed and a fracture filled with calcite runs parallel to the sandstone filling (between the sandstone and the wall rock) through the whole sample. The calcite filled fracture is made up of two pulses of calcite (MnO= 1.15–1.65%, with additional corrensite) growth and quartz clasts form the sandstone are found within the calcite filling which shows that the calcite formed later the emplacement of the sandstone in the fracture. This is also supported by a thin calcite filled fracture cutting through the sandstone in the middle of the fracture and that calcite has entered the sandstone as cement close to the wall rock contact and in the sandstone apophyses in the wall rock. Chlorite and K-feldspar are found between the wall rock and the calcite filling. The sandstone is made up of rounded clasts of quartz and subordinate less rounded K-feldspar crystals, and less common magnetite (partly replaced by hematite), ilmenite and titanite. The most coarse-grained quartz clasts are only found in the middle of the filling and there is a gradual reduction of the clast size towards the rims of the filling. The amounts of matrix (fine-grained quartz, K-feldspar and clay minerals) and the amount of clay minerals are also increased towards the wall rock contacts. The wall rock is quite fresh (e.g. fresh biotite).

Thin section 2:
This thin section show similar features as KLX11D – 30.410–30.798 m (1). However, in this thin section calcite filled fractures (MnO= 1.15–1.65 %, with additional REE-carbonate) and hematite is found at the rims of the sandstone filling.

Photograph of sample KLX11D: 30.410–30.798 m (sandstone- and calcite-filled fracture).

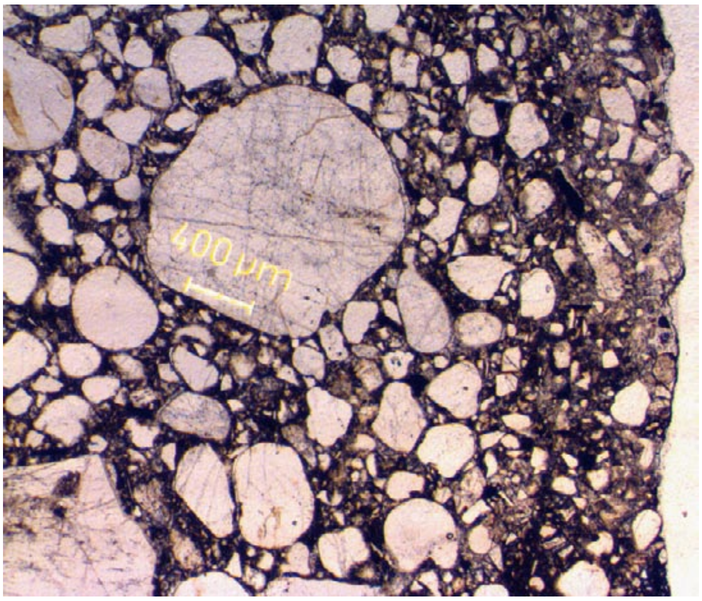

KLX11D: 30.410–30.798 m (photomicrograph of sandstone).

KLX11D: 64.336–64.892 m

Minerals: Chlorite, K-feldspar, albite, epidote, quartz, clay minerals, hematite ,illlite, mixed-layer clay (smectite/illite-dominated, swelling), (kaolinite, goethite and barite).

The wall rock is heavily altered in the whole sample. Magnetite is partly replaced by hematite (~50 % replacement). All biotite is replaced by chlorite and all plagioclase is pseudomorphed by albite, K-feldspar, sericite and hematite, which give the rock a heavily red-stained appearance. The red-staining is not increased towards the fracture. Quartz is dissolved and the resulting voids are partly (sometimes completely) filled with calcite, K-feldspar (adularia), albite and epidote, which indicates that the alteration occurred at temperatures higher than ~250°C.

Photograph of sample KLX11D: 64.336–64.892 m.

KLX11D: 96.150–96.290 m

Minerals: Calcite, mixed-layer clay, pyrite (cubic, fresh) and chalcopyrite.

Photograph of sample KLX11D: 96.150–96.290 m.

KLX11D: 108.600–108.810 m

Minerals: Chlorite, clay minerals, illite, calcite, pyrite, hematite and chalcopyrite.

Photograph of sample KLX11D: 108.600–108.810 m (fracture surfaces with e.g. chlorite hematite and goethite).

KLX11E: 1.840–1.890 m

Minerals: Chlorite, clay minerals, kaolinite, quartz, hematite and/or goethite, K-feldspar and plagioclase.

Photograph of sample KLX11E: 1.840–1.890 m (fracture surface with e.g. goethite).

KLX11E: 4.405–4.535 m

Minerals: Chlorite, quartz, K-feldspar, plagioclase, mixed-layer clay (smectite/illite-rich, swelling), (kaolinite and possibly goethite).

Photograph of sample KLX11E: 4.405–4.535 m (fracture surface with e.g. chlorite and goethite).

KLX11E: 19.530–19.972 m

Minerals: Chlorite, K-feldspar, albite,calcite, REE-carbonate, (rutile and possibly goethite – diffuse XRD peaks).

Photograph of sample KLX11E: 19.530–19.972 m.

KLX11E: 21.465–21.520 m

Minerals: Mixed-layer clay (occasionally very Fe-rich), biotite, quartz, REE-carbonate (Ce rich) and hematite.

Photograph of sample KLX11E: 21.465–21.520 m (fracture surface with e.g. chlorite and goethite).

KLX11E: 42.345–42.451 m

Minerals: Chlorite, clay minerals and calcite.

Photograph of sample KLX11E: 42.345–42.451 m (fracture surfaces with e.g. chlorite).

KLX11E: 59.870–60.148 m

Minerals: Calcite, hematite, galena, sphalerite, chalcopyrite, pyrite and mixed-layer clay.

Photograph of sample KLX11E: 59.870–60.148 m (fracture surfaces with calcite).

KLX11E: 72.940–73.059 m

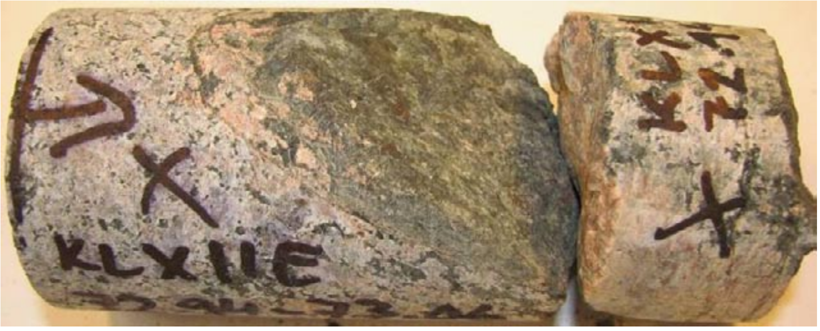

Photograph of sample KLX11E: 72.940–73.059 m.

KLX11E: 98.820–98.889 m

Minerals: Calcite (scalenohedral), harmotome (euhedral), chlorite, hematite, pyrite (cubic, fresh), (and galena).

Photograph of sample KLX11E: 98.820–98.889 m (fracture surface with e.g. calcite and chlorite).

KLX11E: 109.000–109.114 m

1–2 cm wide sandstone filling in a somewhat undulating fracture. Open fractures are found at both of the wall rock contacts. One of the fracture surfaces of these open fractures are covered by illite, mixed layer clay, pyrite (fresh, cubic), quartz, REE-carbonate and K-feldspar. The sandstone filling is very fine-grained, greenish in colour and is composed of chlorite, mixed-layer clay, quartz, K-feldspar and illite (dominates in the most fine-grained parts), along with wall rock fragments (mostly fine-grained, angular quartz, and subordinate, chlorite, K-feldspar and plagioclase). The fine-grained illite dominated parts are most frequent at the rim of the filling but these fine-grained parts also extend into the centre of the filling. Opaque minerals (quite low amount) in the filling are fresh magnetite, magnetite partly replaced by hematite and pyrite.

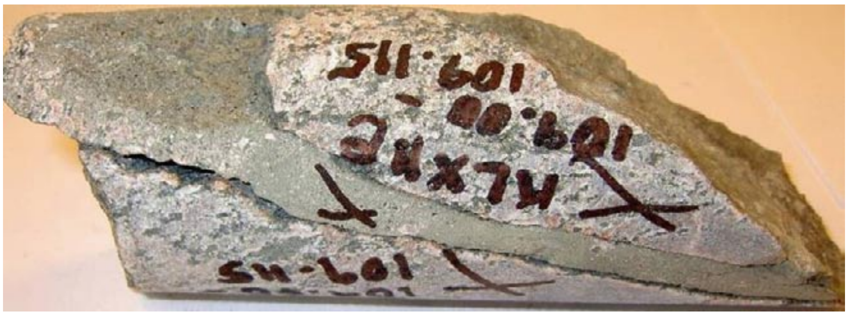

Photograph of sample KLX11E: 109.000–109.114 m (fracture filled with sandstone, very rich in illite and clay minerals).

KLX11E: 113.210–113.379 m

The wall rock is heavily altered in the whole sample. The fracture is coated by calcite (MnO= <0.1 wt %) and K-feldspar. This fracture is also penetrating into the wall rock showing that the presently open fracture is a re-activated older fracture. Magnetite is partly replaced by hematite (~50 % replacement). All biotite is replaced by chlorite and all plagioclase is pseudomorphed by albite, K-feldspar, sericite and hematite, which give the rock a heavily red-stained appearance. The red-staining is not increased towards the fracture. Quartz is dissolved and the resulting voids are partly (sometimes completely) filled with calcite, K-feldspar (adularia), albite, chlorite, apatite and epidote, which indicates that the alteration occurred at temperatures higher than ~250°C.

Photograph of sample KLX11E: 113.210–113.379 m.

KLX11E: 117.090–117.279 m

The sandstone filling is 5 mm wide and one of the rims is bordered by an open fracture. This fracture surface is covered with pyrite (quite fresh), calcite (scalenohedral), quartz, mixed layer clay, REE-carbonate and illite. Thin calcite coatings (MnO= 0 %, pyrite and mixed layer clay is included in the coatings) are found on both of the rims of the sandstone filling. The sandstone filling is greenish in colour, very fine-grained and the matrix is composed of illite, calcite, chlorite, quartz and K-feldspar. Quartz clasts and fragments are dominantly angular but rounded quartz clasts are also abundant. Angular fragments of plagioclase, K-feldspar, chlorite and epidote also exist. The sandstone filling is gradually more fine-grained towards the wall rock rim. Rounded clasts are found to a slightly higher degree in the centre of the filling than in the rest of the filling. Opaque minerals in the filling are fresh magnetite, pyrite and chalcopyrite. The wall rock is fine-grained, slightly foliated and red-stained. The plagioclase alteration and red-staining intensity is not increased towards the fracture. Biotite is partly replaced by chlorite. The magnetite and the low amount of pyrite in the wall rock are fresh.

Photograph of sample KLX11E: 117.090–117.279 m (sandstone filled fracture).

KLX11E: 120.830–120.915 m

Minerals: Mixed-layer clay (sometimes very Fe-rich), chlorite, pyrite (cubic, fresh), hematite, calcite, K-feldspar, illite and apatite.

Photograph of sample KLX11E: 120.830–120.915 m (fracture surfaces with pyrite crystals on hematite-stained surface).

KLX11F: 2.350–2.585 m

Minerals: Chlorite, clay minerals and goethite.

Photograph of sample KLX11F: 2.350–2.585 m (fracture surface with e.g. goethite).

KLX11F: 6.631–6.691 m

Undulating fracture with rather smooth surface covered with mixed-layer clay (sometimes very Fe-rich), illite, chlorite, biotite, hematite/FeOOH, quartz, plagioclase, REE-carbonate and trace amounts of Zn. Pyrite and magnetite are fresh in the whole section. However, pyrite is not found closer than 0.5 mm from the fracture. The biotite is mostly fresh but is somewhat altered within 0.5 mm of the fracture. Plagioclase is partly altered in the whole sample.

Photograph of sample KLX11F: 6.631–6.691 m (fracture surface with e.g. goethite).

KLX11F: 9.590–9.690 m

Minerals: Illite, chlorite, clay minerals, K-feldspar, REE-carboante, hematite and/or goethite, albite, Ce, and quartz.

Photograph of sample KLX11F: 9.590–9.690 m (fracture surfaces with e.g. goethite).

KLX11F: 15.280–15.485 m

Minerals: Quartz, plagioclase, K-feldspar, calcite, REE-carbonater, chlorite, mixed-layer clay (vermiculite- smectite-dominated), and possibly goethite.

Photograph of sample KLX11F: 15.280–15.485 m (fracture surfaces with e.g. goethite and calcite).

KLX11F: 17.160–17.430 m

Minerals: Illite, mixed-layer clay, chlorite, quartz, hematite, K-feldspar, epidote, plagioclase and REE-carbonate.

Photograph of sample KLX11F: 17.160–17.430 m (fracture surfaces).

KLX11F: 20.221–20.361 m

Minerals: Pyrite (altered), calcite, mixed-layer clay, illite, hematite (and galena).

Photograph of sample KLX11F: 20.221–20.361 m (fracture surface with e.g. calcite).

KLX11F: 52.340–52.570 m

Minerals: Chlorite, K-feldspar, corrensite, quartz, plagioclase, calcite and possibly goethite.

Photograph of sample KLX11F: 52.340–52.570 m.

KLX11F: 70.170–70.430 m

Minerals: Chlorite, calcite, mixed-layer clay (smectite- and illite dominated), quartz, K-feldspar, hematite and possibly goethite.

Photograph of sample KLX11F: 70.170–70.430 m.

KLX11F: 111.380–111.490 m

Minerals: K-feldspar, albite, mixed-layer clay, calcite, REE-carbonate and pyrite (fresh).

Photograph of sample KLX11F: 111.380–111.490 m.

Appendix 2

Chemical analyses

Chemical analyses

Borehole		**KLX09B**	**KLX09C**	**KLX09D**	**KLX09D**	**KLX09D**
Sample (m)		**11.112–11.322**	**84.999–85.120**	**3.700–3.860**	**9.460–9.610**	**12.869–13.112**
SiO_2	%	43.3	45.6	46.2	56.6	44.8
Al_2O_3	%	12.7	16	18.2	16.3	13.9
CaO	%	13.1	5.16	5.14	2.55	2.58
Fe_2O_3	%	5.37	11.2	7.51	7.28	12.6
K_2O	%	3.6	8.02	2.95	6.81	4.74
MgO	%	2.99	4.51	3.82	2.38	6.88
MnO	%	0.26	0.17	0.84	0.1	0.15
Na_2O	%	2.48	0.44	0.38	1.31	0.32
P_2O_5	%	0.22	0.24	0.08	0.38	0.08
TiO_2	%	0.67	0.87	0.14	0.81	0.17
Total	%	84.7	92.2	85.3	94.5	86.2
Ba	mg/kg	20,300	589	5,920	1,970	1,770
Be	mg/kg	7.91	46.2	19.3	24.1	34.9
Co	mg/kg	< 6	22.5	14	11.8	10.4
Cr	mg/kg	24.9	94.6	13.9	42.9	17.8
Cs	mg/kg	4.22	16.4	8.56	15.6	5.93
Cu	mg/kg	14.2	6.17	69.7	317	55.5
Ga	mg/kg	17	29.2	25.1	18.2	20.3
Hf	mg/kg	5.71	4.91	3.22	8.84	2.58
Mo	mg/kg	< 2	< 2	3.43	< 2	< 2
Nb	mg/kg	9.18	9.34	3.47	16.1	4.16
Ni	mg/kg	20.4	35.1	< 10	20	< 10
Rb	mg/kg	139	331	78.1	210	124
Sc	mg/kg	8.45	24.9	3.52	12.1	2.34
Sn	mg/kg	3.67	6.18	13	25.2	5.66
Sr	mg/kg	419	114	120	312	135
Ta	mg/kg	1.06	0.99	0.28	1.74	0.59
Th	mg/kg	4.4	9.32	2.3	14.8	2.63
U	mg/kg	4.09	5.92	2.6	8.11	5.63
V	mg/kg	90.5	85.9	80.8	141	167
W	mg/kg	1.8	12.3	2.96	5.74	1.2
Y	mg/kg	17.5	23.8	7.73	39.6	7.24
Zn	mg/kg	142	276	229	811	214
Zr	mg/kg	189	168	107	294	77.4
La	mg/kg	108	65.5	32.9	263	47.1
Ce	mg/kg	152	121	94.3	423	116
Pr	mg/kg	16.1	12.9	6.8	39.4	7.45
Nd	mg/kg	58.7	50.4	24.3	146	25.5
Sm	mg/kg	8.47	9.8	3.49	18.8	3.29
Eu	mg/kg	2.11	2.42	0.92	3.8	0.66
Gd	mg/kg	5.7	7.22	2.28	12	2.27
Tb	mg/kg	0.62	0.94	0.26	1.34	0.26
Dy	mg/kg	3.52	5.2	1.48	7.09	1.45
Ho	mg/kg	0.64	0.99	0.29	1.35	0.28
Er	mg/kg	1.93	2.55	0.87	3.81	0.74
Tm	mg/kg	0.27	0.38	0.13	0.53	< 0.1
Yb	mg/kg	1.84	2.6	0.98	3.63	0.83
Lu	mg/kg	0.28	0.37	0.19	0.54	0.16

Chemical analyses

Borehole		**KLX09D**	**KLX09D**	**KLX09D**	**KLX09E**	**KLX09E**	**KLX09F**
Sample (m)		**83.015–83.180**	**88.430–88.754**	**104.592–104.868**	**8.910–9.010**	**11.450–11.650**	**12.90–13.06**
SiO_2	%	37.4	49.5	56.6	46.9	50.8	53.5
Al_2O_3	%	16.8	21.6	8.95	13.8	14.8	17.7
CaO	%	6.09	1.66	10.2	2.66	1.85	2.02
Fe_2O_3	%	14.8	8.77	6.63	8.42	9.53	5.38
K_2O	%	3.87	8.41	2.1	3.79	7.18	4.96
MgO	%	7.95	2.98	3.29	3.59	7.1	6.08
MnO	%	0.34	0.12	0.2	6.27	0.19	0.16
Na_2O	%	0.07	0.68	1.84	2.7	0.71	1.77
P_2O_5	%	0.22	0.09	0.11	0.45	0.34	0.19
TiO_2	%	1.21	0.35	0.41	0.79	0.82	0.49
Total	%	88.7	94.2	90.3	89.4	93.3	92.2
Ba	mg/kg	212	1,150	407	6,090	1,770	2,060
Be	mg/kg	62.9	45.6	22.3	35.1	20.4	26
Co	mg/kg	39.5	10.1	17.9	107	33.4	< 6
Cr	mg/kg	223	61.9	90	114	40.3	22.2
Cs	mg/kg	41.3	55.1	13.9	10.7	17.4	20.9
Cu	mg/kg	32.9	65.1	35	458	60.8	54.6
Ga	mg/kg	48.3	28.4	14.1	18.8	23.4	26.3
Hf	mg/kg	5.21	3.81	2.91	6.73	5.79	4.85
Mo	mg/kg	< 2	< 2	< 2	11.6	< 2	< 2
Nb	mg/kg	17	8.62	5.46	11.7	14.8	11.4
Ni	mg/kg	45.2	17.4	39	36.9	29.2	14.6
Rb	mg/kg	430	990	148	174	283	177
Sc	mg/kg	19.6	15.7	14.4	15.7	12	8.81
Sn	mg/kg	6.93	10.7	4.51	8.24	3.56	9.49
Sr	mg/kg	64.2	67.8	267	675	203	205
Ta	mg/kg	1.09	0.72	0.38	1.11	1.25	1.07
Th	mg/kg	8.66	11.3	10.9	8.31	6.66	20.7
U	mg/kg	25.3	8.76	3.58	9.59	5.24	15
V	mg/kg	125	152	76.4	141	138	104
W	mg/kg	12.8	12.8	2.39	38.9	5.52	3.91
Y	mg/kg	75.5	18.5	18.7	31.6	24	28.3
Zn	mg/kg	237	121	212	286	360	376
Zr	mg/kg	169	104	105	271	222	155
La	mg/kg	59	15.1	70.9	148	76.6	345
Ce	mg/kg	177	30.2	138	341	150	434
Pr	mg/kg	27.9	3.91	14.6	28.4	16.3	44.7
Nd	mg/kg	126	19.3	48.9	94.6	56.8	147
Sm	mg/kg	24.5	5.42	7.97	14	8.82	15.3
Eu	mg/kg	5.66	1.39	1.57	3.4	1.93	2.66
Gd	mg/kg	18.2	5.1	5.69	10	6	9.18
Tb	mg/kg	2.51	0.66	0.78	1.11	0.77	0.89
Dy	mg/kg	14.2	3.79	4.28	5.75	4.35	4.82
Ho	mg/kg	2.73	0.73	0.75	1.05	0.76	0.93
Er	mg/kg	7.9	1.86	1.82	3.08	2.13	2.52
Tm	mg/kg	1.13	0.26	0.24	0.45	0.35	0.35
Yb	mg/kg	8.22	2	1.6	3.21	2.27	2.31
Lu	mg/kg	1.26	0.29	0.24	0.51	0.35	0.33

Chemical analyses

Borehole		KLX09F	KLX09F	KLX09F	KLX09F	KLX09F	KLX09G
Sample (m)		**58.81–59.05**	**68.53–68.72**	**79.66–79.87**	**81.78–81.89**	**135.23–135.33**	**40.358–40.415**
SiO_2	%	11.6	48.7	57.7	39.1	51.5	31.6
Al_2O_3	%	3.4	14.9	16.9	16.8	14.9	11.3
CaO	%	40.5	7.88	2.26	4.31	3.76	19.8
Fe_2O_3	%	3.82	8.09	5.47	16.3	12	8.51
K_2O	%	0.895	5.03	4.75	5.5	4.52	4.39
MgO	%	1.67	2.48	4.22	7.04	4.06	2.21
MnO	%	0.51	0.11	0.19	0.2	0.15	0.24
Na_2O	%	0.41	1.56	2.62	0.82	1.95	0.64
P_2O_5	%	0.04	0.15	0.19	0.28	0.31	0.21
TiO_2	%	0.07	0.34	0.47	1.1	0.77	0.47
Total	%	62.9	89.2	94.8	91.4	93.9	79.4
Ba	mg/kg	351	11,400	937	409	1,610	1,410
Be	mg/kg	15	11.6	41.5	19.5	14	13.7
Co	mg/kg	< 10	< 6	9.86	26	14.4	7.83
Cr	mg/kg	< 20	15.6	23.8	247	34.7	30
Cs	mg/kg	1.11	18.9	17.8	25.6	31.2	17
Cu	mg/kg	< 10	10.3	< 6	< 6	< 6	20.3
Ga	mg/kg	6.63	21.3	30.5	31.4	22.5	15.8
Hf	mg/kg	4.01	4.59	6.28	4.39	7.7	4.26
Mo	mg/kg	< 4	< 2	< 2	2.59	< 2	< 2
Nb	mg/kg	2.53	9.13	9.32	10	14.4	7.43
Ni	mg/kg	< 20	< 10	13.2	48.1	17.2	< 10
Rb	mg/kg	28.9	212	250	413	259	169
Sc	mg/kg	< 2	4.27	7.33	34.3	10.8	8.51
Sn	mg/kg	2.42	4.64	4.98	6	5.62	4.2
Sr	mg/kg	192	213	706	115	508	488
Ta	mg/kg	0.59	0.92	1.08	0.6	1.48	0.69
Th	mg/kg	1.29	6.79	9.18	7	9.75	5.21
U	mg/kg	3.07	3.13	13.1	29	4.72	43
V	mg/kg	22.4	55.2	64.5	186	105	132
W	mg/kg	1.55	6.01	3.02	11.4	1.93	4.15
Y	mg/kg	5.05	10.7	18.4	22.8	22.6	18.3
Zn	mg/kg	196	92.7	158	333	607	150
Zr	mg/kg	82.4	134	213	151	275	148
La	mg/kg	173	83.4	75.9	121	47.3	120
Ce	mg/kg	142	117	121	157	109	183
Pr	mg/kg	9.9	11.3	13	17.8	13.4	19.8
Nd	mg/kg	30.3	37.6	45.2	68.1	50.8	74.6
Sm	mg/kg	2.34	4.5	6.67	10.5	8.21	8.85
Eu	mg/kg	0.47	1.02	1.27	2.19	1.69	1.86
Gd	mg/kg	1.27	2.79	4.54	7.55	5.68	5.67
Tb	mg/kg	< 0.2	0.37	0.6	0.84	0.71	0.57
Dy	mg/kg	0.67	1.9	3.55	4.31	4.1	3.09
Ho	mg/kg	0.14	0.36	0.69	0.82	0.81	0.6
Er	mg/kg	0.37	1.14	1.94	2.02	2.22	1.56
Tm	mg/kg	< 0.2	0.19	0.29	0.28	0.32	0.21
Yb	mg/kg	0.49	1.22	2.03	2.08	2.18	1.53
Lu	mg/kg	0.09	0.22	0.3	0.31	0.33	0.24

Chemical analyses

Borehole		KLX11B	KLX11B	KLX11C	KLX11D	KLX11D	KLX11D
Sample (m)		**3.480–3.71**	**13.237–13.5**	**13.481–13.591**	**0.930–1.030**	**2.020–2.060**	**29.670–30.148**
SiO_2	%	43.9	50.5	52.4	47	60	57.6
Al_2O_3	%	15	15.7	16.9	11.8	15.5	11.7
CaO	%	1.17	7.32	3.88	2.49	3.58	3.2
Fe_2O_3	%	9.72	9.01	9.12	11.5	6.37	9.08
K_2O	%	3.61	4.08	6.4	4	4.26	5.78
MgO	%	1.59	3.7	3.75	9.44	2.66	4.89
MnO	%	0.06	0.24	0.31	0.42	0.12	0.25
Na_2O	%	1.26	1.44	1.58	0.82	2.83	0.65
P_2O_5	%	0.73	0.3	0.1	0.42	0.3	0.22
TiO_2	%	0.52	0.89	0.41	1.26	1.16	0.73
Total	%	77.6	93.2	94.8	89.2	96.8	94.1
Ba	mg/kg	706	1,840	1,150	409	1,100	841
Be	mg/kg	1.86	6.72	3.27	1.62	2.39	20.4
Co	mg/kg	14.5	17.1	22.2	19.7	11.8	22.3
Cr	mg/kg	48.4	29.1	23.5	53.6	43.2	94.9
Cs	mg/kg	4.56	5.42	1.94	16.9	2.86	6.9
Cu	mg/kg	27	43.8	10.8	21	24.1	8.03
Ga	mg/kg	13.6	20.4	19	19.6	17.2	18.1
Hf	mg/kg	4.71	3.28	4.53	12.2	4.46	12.6
Mo	mg/kg	3.09	< 2	< 2	< 3	< 2	< 2
Nb	mg/kg	11	15.3	7.01	16.2	14.4	9.19
Ni	mg/kg	19.9	16.7	23.3	17.4	16.3	18.8
Rb	mg/kg	117	119	189	221	146	115
Sc	mg/kg	12	11.2	10.4	16.6	14.8	33.4
Sn	mg/kg	2.75	4.06	2.49	3.61	3.96	3.33
Sr	mg/kg	257	232	344	119	525	117
Ta	mg/kg	1.5	1.1	0.56	1.16	1.4	1.09
Th	mg/kg	26.8	8.96	2.26	3.81	7.15	7.06
U	mg/kg	9.96	3.53	2.73	2.92	4.2	3.55
V	mg/kg	90.3	121	110	153	111	145
W	mg/kg	3.77	4.06	6.45	63.9	2.43	9.88
Y	mg/kg	48.3	27.2	16.5	33.7	28.7	104
Zn	mg/kg	114	195	331	206	93	451
Zr	mg/kg	155	113	169	454	140	463
La	mg/kg	348	69.1	185	164	57.6	245
Ce	mg/kg	711	132	275	297	126	425
Pr	mg/kg	61.4	13.2	18.7	27.9	13.2	45.7
Nd	mg/kg	201	47.6	56.2	95.5	47.3	172
Sm	mg/kg	27.2	7.44	5.98	11.7	7.86	29.2
Eu	mg/kg	3.7	2.04	1.47	2.17	1.78	6.39
Gd	mg/kg	17.2	5.87	4.13	8.53	6.42	29.6
Tb	mg/kg	2.25	0.78	0.57	1.12	0.85	3.89
Dy	mg/kg	12.1	4.87	3.1	6.01	5.23	21.3
Ho	mg/kg	2.06	0.96	0.6	1.19	1.11	4.2
Er	mg/kg	5.37	2.83	1.74	3.44	3.13	10.8
Tm	mg/kg	0.74	0.44	0.22	0.48	0.42	1.29
Yb	mg/kg	4.47	3.05	1.67	3.17	3.09	7.71
Lu	mg/kg	0.56	0.44	0.25	0.48	0.42	1.06

Chemical analyses

Borehole		KLX11D	KLX11D	KLX11D	KLX11E	KLX11E	KLX11E
Sample (m)		64.336–64.892R	64.336–64.892G	108.600–108.81	1.840–1.890	4.405–4.535	19.530–19.972
SiO_2	%	49.4	46.6	43.6	40.2	40.2	32.6
Al_2O_3	%	18.8	15.7	14.1	15.4	15.9	14.1
CaO	%	6.95	3.35	8.47	2.21	1.5	7.15
Fe_2O_3	%	9.68	14.3	12.3	10.2	23.1	19.1
K_2O	%	5.63	6.05	4.64	1.81	3.43	1.96
MgO	%	2.19	5.23	3.61	2.49	4.25	9.06
MnO	%	0.09	0.19	0.14	0.27	0.36	0.34
Na_2O	%	0.9	1.36	2	1.31	0.86	0.5
P_2O_5	%	0.14	0.41	0.24	0.78	0.13	1.24
TiO_2	%	0.59	0.95	0.82	1.21	0.45	4.21
Total	%	94.4	94.1	89.9	75.9	90.2	90.3
Ba	mg/kg	485	717	646	492	1100	250
Be	mg/kg	14.1	6.97	14.1	2.19	5.39	3.05
Co	mg/kg	9.33	33.4	23.4	26.8	65.8	38.8
Cr	mg/kg	27.8	76	34.2	110	26.4	28
Cs	mg/kg	63	36.8	15	4.65	3.13	2.21
Cu	mg/kg	23.7	18.6	156	70.4	58.8	14.8
Ga	mg/kg	38.3	28.9	20.8	13.9	38.2	50.1
Hf	mg/kg	3.09	14	6.81	9.74	2.99	55.4
Mo	mg/kg	< 2	< 2	< 2	3.26	< 2	2.62
Nb	mg/kg	7.3	11.8	13.2	17	6.29	59.5
Ni	mg/kg	< 10	30.9	19.4	30	33.8	26
Rb	mg/kg	380	232	206	110	128	69.1
Sc	mg/kg	25.1	25.5	26.5	14.2	44.1	20.1
Sn	mg/kg	5.87	7.44	6.33	6.71	6.06	7.6
Sr	mg/kg	2,700	403	118	230	93.6	536
Ta	mg/kg	0.64	0.82	1.3	1.59	0.58	5.28
Th	mg/kg	4.53	16.1	10.6	15.2	4.45	263
U	mg/kg	3.35	6.48	13.6	9.36	1.39	23.2
V	mg/kg	206	184	156	136	206	121
W	mg/kg	5.36	10.4	12	3.87	4.07	4.32
Y	mg/kg	32.1	34.1	50.9	45.7	51.5	120
Zn	mg/kg	101	262	4,700	118	584	524
Zr	mg/kg	99.9	524	207	320	92.5	1,860
La	mg/kg	264	88.7	35.7	91.7	45.6	766
Ce	mg/kg	508	174	66.6	267	93.3	1,540
Pr	mg/kg	58.9	20.2	9.15	23	13.2	150
Nd	mg/kg	212	73.3	44.9	86.4	56.9	465
Sm	mg/kg	25.6	11.8	13	15.6	12.7	57.8
Eu	mg/kg	4.17	2.54	3.46	3.45	2.82	4.27
Gd	mg/kg	13	9.46	14.7	11.3	12.4	37.2
Tb	mg/kg	1.24	1.21	1.79	1.77	2.01	4.51
Dy	mg/kg	6.33	7.12	10.2	10.9	12	24.2
Ho	mg/kg	1.16	1.38	1.79	1.95	2.44	4.82
Er	mg/kg	3.18	3.93	4.93	5.68	7.07	13.4
Tm	mg/kg	0.54	0.6	0.65	0.78	1.16	1.94
Yb	mg/kg	4.05	4.29	4.35	5.76	9.37	12.9
Lu	mg/kg	0.7	0.69	0.57	0.78	1.4	1.94

Chemical analyses

Borehole		KLX11E	KLX11F	KLX11F	KLX11F	KLX11F	KLX11F
Sample (m)		**42.345–42.451**	**2.35–2.585**	**9.59–9.69**	**15.280–15.485**	**52.34–52.57**	**70.170–70.430**
SiO_2	%	35	55.1	46	52.5	39.1	26
Al_2O_3	%	11.8	14	11	14.6	11.8	10.8
CaO	%	9.1	2.52	2.24	2.64	1.68	15.7
Fe_2O_3	%	15.2	8.83	12.5	8.72	13.8	18.6
K_2O	%	0.64	5.62	2.34	7.8	1.91	2.31
MgO	%	13.1	4.59	9.98	4.83	18.2	5.07
MnO	%	0.27	0.23	0.24	0.16	0.2	0.27
Na_2O	%	0.09	2.15	1.01	0.47	0.34	0.62
P_2O_5	%	0.01	0.42	0.15	0.06	0.03	0.12
TiO_2	%	0.04	0.87	0.5	0.42	0.09	0.53
Total	%	85.3	94.3	86	92.2	87.2	80
Ba	mg/kg	170	688	569	388	114	293
Be	mg/kg	6.61	2.03	2.35	5.94	1.14	13.9
Co	mg/kg	25.2	15.5	15.1	9.73	26.3	24.5
Cr	mg/kg	15.7	39.2	32.7	86.2	17.6	42.2
Cs	mg/kg	1.59	3.79	6.92	14.5	0.67	19.2
Cu	mg/kg	15.9	74.9	58.2	113	31.7	48.8
Ga	mg/kg	41.8	20.4	18.2	22.9	17.5	20.4
Hf	mg/kg	1.41	6.99	3.08	1.43	0.858	5.23
Mo	mg/kg	< 2	< 2	< 2	< 2	< 2	< 2
Nb	mg/kg	1.13	10.9	10.2	8.98	2.29	8.16
Ni	mg/kg	30.1	16	< 10	17	12.9	21.9
Rb	mg/kg	15.9	150	70.4	218	32.6	106
Sc	mg/kg	< 1	17.1	8.36	22.5	6.05	37.9
Sn	mg/kg	2.08	9.26	2.82	5.93	2.37	8.28
Sr	mg/kg	1100	152	117	284	106	89
Ta	mg/kg	0.25	0.86	0.76	0.49	0.28	0.7
Th	mg/kg	1.85	8.97	15.1	4.3	1.53	10.2
U	mg/kg	0.77	7.24	5.97	3.64	1.13	6.12
V	mg/kg	103	111	117	197	90.3	250
W	mg/kg	2.63	3.59	7.99	7.48	1.18	15.4
Y	mg/kg	8.55	22.1	25.1	18	4.59	76.6
Zn	mg/kg	292	134	576	290	389	981
Zr	mg/kg	10.1	233	93.9	36.5	16.7	175
La	mg/kg	64.8	77.6	507	131	9.62	94.7
Ce	mg/kg	62.6	147	860	332	16.5	156
Pr	mg/kg	4.95	13.4	73.6	29.1	1.74	18
Nd	mg/kg	15.5	44.5	212	91	6.44	69.9
Sm	mg/kg	1.93	6.59	19.7	12.6	1.22	15
Eu	mg/kg	0.41	1.52	1.9	2.15	0.26	3.82
Gd	mg/kg	1.82	5.39	9.2	7.51	1.09	16
Tb	mg/kg	0.24	0.7	0.94	0.88	0.15	2.54
Dy	mg/kg	1.34	4.15	4.59	4.76	0.76	14.5
Ho	mg/kg	0.27	0.83	0.84	0.81	0.17	2.62
Er	mg/kg	0.77	2.44	2.47	2.16	0.43	7.21
Tm	mg/kg	< 0.1	0.34	0.32	0.31	< 0.1	0.94
Yb	mg/kg	0.72	2.42	2.19	2.08	0.39	5.79
Lu	mg/kg	0.12	0.37	0.32	0.37	0.07	0.76

Appendix 3

U-series analyses

U-series analyses

Borehole	Sample	^{238}U	Error 1σ	^{234}U	Error 1σ	^{230}Th	Error 1σ	^{232}Th	Error 1σ	^{234}U/^{238}U	Error 1σ	^{230}Th/^{234}U	Error 1σ
KLX09B	7.18–7.29 m	117	2	155	3	210	10	68	5	1.32	0.04	1.36	0.07
KLX09B	11.112–11.322 m	76	1	88	1	96	5	53	3	1.15	0.02	1.09	0.06
KLX09C	84.999–85.120 m	75	2	87	2	86	6	56	5	1.17	0.03	0.99	0.08
KLX09D	3.700–3.860 m	36	1	42	1	85	3	19	1	1.18	0.03	2.01	0.08
KLX09D	83.015–83.180 m	321	1	396	2	293	13	53	4	1.23	0.01	0.74	0.03
KLX09D	88.430–88.754 m	119	2	128	2	123	5	61	3	1.07	0.02	0.96	0.04
KLX09D	104.592–104.868 m	53	1	60	1	62	2	57	2	1.13	0.02	1.03	0.03
KLX09E	1.005–1.145 m	76	1	79	1	96	9	61	7	1.03	0.02	1.21	0.12
KLX09E	11.450–11.650 m	60	1	67	1	78	3	45	2	1.12	0.03	1.16	0.04
KLX09F	68.53–68.72 m	39	1	48	1	45	1	31	1	1.21	0.04	0.95	0.04
KLX09F	79.66–79.87 m	180	2	239	3	201	5	59	2	1.32	0.02	0.84	0.02
KLX09F	81.78–81.89 m	460	2	677	3	656	21	45	4	1.47	0.01	0.97	0.03
KLX09G	40.358–40.415 m	592	6	964	8	794	10	36	1	1.63	0.02	0.82	0.01
KLX11B	3.480–3.710 m	126	2	136	2	152	3	130	2	1.08	0.02	1.11	0.03
KLX11B	13.237–13.500 m	38	1	41	1	70	2	40	1	1.08	0.03	1.68	0.05
KLX11D	2.020–2.060 m	71	1	74	1	80	2	48	2	1.04	0.02	1.08	0.03
KLX11D	64.336–64.892 mG	43	1	51	1	76	5	63	4	1.21	0.03	1.48	0.1
KLX11D	108.600–108.810 m	248	2	296	2	324	8	93	4	1.19	0.01	1.09	0.03
KLX11E	4.405–4.535 m	23	1	23	1	37	3	48	3	1.02	0.03	1.57	0.12
KLX11E	19.530–19.972 m	292	3	281	3	447	34	1,115	67	0.96	0.01	1.59	0.12
KLX11E	42.345–42.451 m	10	1	12	1	28	1	15	1	1.25	0.06	2.23	0.09
KLX11F	2.35–2.585 m	108	1	111	1	107	9	43	5	1.03	0.01	0.96	0.08

Appendix 4

δ^{13}C, δ^{18}O, ^{87}Sr/^{86}Sr in calcite and δ^{34}S in pyrite

δ^{13}C, δ^{18}O, ^{87}Sr/^{86}Sr in calcite and δ^{34}S in pyrite

Borehole	SecUp (m)	SecLow (m)	δ^{13}C ‰ $_{PDB}$	δ^{18}O ‰ $_{PDB}$	^{87}Sr/^{86}Sr	δ^{34}S ‰ $_{CDT}$
KLX09C	29.738	29.863	–0.8	–7.168		
KLX09C	44.965	45.258	–10.136	–8.554		
KLX09C	47.202	47.383	–10.44	–8.013		
KLX09C	117.384	117.545				41.4
KLX09D	7.11	7.34	–6.318	–9.926		
KLX09D	19.892	20.003	–11.528	–7.78		
KLX09D	23.168	23.441	–7.476	–8.499		23.4
KLX09D	29.786	29.917	–15.297	–6.759	0.716457	
KLX09D	32.025	32.176	–34.293	–5.356		
KLX09E	31.959	32.14	–32.215	–5.832	0.716294	
KLX09E	71.515	71.916	–9.637	–8.721		
KLX09F	9.9	10	–9.655	–11.405		
KLX09F	10.83	10.96	–7.915	–6.391		
KLX09F	22.6	22.79	–8.49	–7.064		
KLX09F	52.24	52.28	–20.726	–7.986		
KLX09F	54.04	54.16	–18.317	–7.113		
KLX09F	64.54	64.72	–8.812	–6.706	0.716194	
KLX09F	76	76.072	–4.481	–6.197	0.716564	
KLX09F	102.26	102.45	–1.488	–6.771	0.715866	
KLX09F	102.26	102.45	–8.881	–7.8		
KLX09F	112.81	112.9	–20.663	–7.873		
KLX09G	40.358	40.415	–13.116	–5.565		
KLX09G	41.168	41.411	–20.03	–8.411		16.8
KLX11B	76.27	76.395	–5.681	–10.363		
KLX11C	5.72	5.98	–14.389	–8.103		
KLX11C	69.91	70.199	–8.811	–10.517		
KLX11C	87.45	87.49	–11.293	–15.393		
KLX11D	0.93	1.03	–11.893	–13.272		
KLX11D	13.74	13.805	–6.38	–6.801		
KLX11D	24.25	24.504	–8.674	–10.723		
KLX11D	30.41	30.798	–6.922	–8.038		
KLX11D	96.15	96.29	–8.766	–16.308		
KLX11D	96.15	96.29	1.367	–7.579		
KLX11E	59.87	60.148	–10.947	–8.078		
KLX11E	98.82	98.889	–9.198	–7.757		
KLX11E	117.09	117.279	–11.938	–8.487		46.9
KLX11E	120.83	120.915				19.8
KLX11F	20.221	20.361	–13.065	–11.626		